Summer 2013

Incorporating sheet-likeness information in intensity-based lung CT image registration

Yang Wook Kim
University of Iowa

INCORPORATING SHEET-LIKENESS INFORMATION IN INTENSITY-BASED LUNG CT IMAGE REGISTRATION

by

Yang Wook Kim

A thesis submitted in partial fulfillment of the
requirements for the Master of Science
degree in Biomedical Engineering
in the Graduate College of
The University of Iowa

August 2013

Thesis Supervisor: Professor Joseph M. Reinhardt

Graduate College
The University of Iowa
Iowa City, Iowa

CERTIFICATE OF APPROVAL

MASTER'S THESIS

This is to certify that the Master's thesis of

Yang Wook Kim

has been approved by the Examining Committee for the thesis requirement for the Master of Science degree in Biomedical Engineering at the August 2013 graduation.

Thesis Committee: _____
Joseph M. Reinhardt, Thesis Supervisor

_____
Gary E. Christensen

_____
Edwin L. Dove

ACKNOWLEDGEMENTS

First of all, I would like to thank my advisor Prof. Reinhardt for his patient guidance and support. I am greatly inspired and impressed by his guidance.

I am very grateful to Prof. Christensen for his wise advice on image registration. I would like to thank Prof. Dove for his comments for the thesis. Thanks to my labmates Kaifang Du, Sandeep Bodduluri, Richard Amendola, Xiayu Xu, and Vinayak Joshi for being helpful and hanging out.

Finally, this thesis is dedicated to my loved parents and family. Their silent support behind me is my biggest motivation.

ABSTRACT

Image registration is a useful technique to measure the change between two or more images. Lung CT image registration is widely used an non-invasive method to measure the lung function changes. Non-invasive lung function measurement accuracy highly depends on lung CT image registration accuracy. Improving the registration accuracy is an important issue.

In this thesis, we propose incorporating information of the anatomical structure of the lung (fissures) as an additional cost function of the lung CT image registration. The intensity-based similarity measurement method (sum of the squared tissue volume differences) is also used to complement lung tissue information matching. However, since fissures are hard to segment, a sheet-likeness filter is applied to detect fissure-like structures. Sheet-likeness is used as an additional cost function of the intensity-based registration. The registration accuracy is verified by the visual assessment and landmark error measurement. The landmark error measurement can show an improvement of the proposed algorithm.

TABLE OF CONTENTS

LIST OF TABLES vi

LIST OF FIGURES vii

CHAPTER

1 INTRODUCTION 1

1.1 Motivation 1
1.2 Organization of the thesis 3

2 BACKGROUND AND RELATED WORK 4

2.1 Background 4
2.1.1 Image Registration 4
2.1.1.1 Point-based method 5
2.1.1.2 Surface-based method 5
2.1.1.3 Intensity-based method 6
2.1.2 Similarity measurement 6
2.1.2.1 Feature (point and/or surface)-based similarity function 6
2.1.2.2 Intensity-based similarity function 7
2.1.2.3 Lung CT image oriented similarity function . . . 11
2.1.3 Related work 11

3 METHODS 26

3.1 Data acquisition 26
3.2 Overall process 26
3.3 Anatomical similarity function 30
3.4 Optimization 39
3.5 Landmark error 39

4 EXPERIMENT RESULTS 42

4.1 Visual assessment 42
4.2 Landmark error 42
4.3 Comparison between cost functions 44

5 DISCUSSION AND CONCLUSION 51

APPENDIX

A ACCUMULATED LANDMARK ERROR 53

B BOX PLOT OF THE LANDMARK ERROR AFTER REGISTRATION 59

REFERENCES 65

LIST OF TABLES

Table

3.1 Applied multiresolution scheme 30

3.2 Object patterns decided by eigenvalues. 34

3.3 The initial landmark error (before registration) and volume ratio between the FRC and TLC image 41

4.1 Mean landmark between before and after the registration with sheet-likeness 44

4.2 Mean landmark error comparison between before and after the registration with various methods (unit : mm) 45

4.3 Minimum landmark error comparison between before and after the registration with various methods (unit : mm) 46

4.4 Maximum landmark error comparison between before and after the registration with various methods (unit : mm) 46

LIST OF FIGURES

Figure

3.1 Segmented FRC and TLC lung images of the H-1 data set. The upper row shows the transverse plane, and the lower row shows the coronal plane. (a) shows FRC image, (b) shows the absolute difference image between FRC and TLC image, and (c) shows TLC image 27

3.2 The entire procedure of the registration 28

3.3 Tissue shape classification measure based on eigenvalues of the image. (a) Line measure. (b) Blob measure. (c) Sheet measure. In this figure, $\lambda_1 \geq \lambda_2 \geq \lambda_3$. Figure from Sato et al. [32]. 32

3.4 Comparison between vesselness and sheet-likeness. The upper row represents the transverse plane, and the lower row represent the coronal plane, (a) shows the vesselness results, (b) shows the fused image between vesselness and sheet-likeness. Red color is used for vesselness, and green color is used for sheet-likeness. Red circles represent the location of the fissures. 35

3.5 Extracted fissure-like structure in FRC. The upper row shows the transverse plane, and the lower row shows the coronal plane, (a) shows the corresponding CT image, and (b) shows the extracted fissure-like structure. The red dotted line represents the location of the fissure. 36

3.6 Extracted fissure-like structure in TLC. The upper row shows the transverse plane, and the lower row shows the coronal plane, (a) shows the corresponding CT image, and (b) shows the extracted fissure-like structure. The red dotted line represents the location of the fissure. 37

3.7 Distribution of the landmark points in the FRC image. Green dots represent each landmark point. Although green dots appear to the outside of the lung, they are located inside of the lung in 3D space. More than 100 well distributed points are used for each data pair. 40

4.1 Comparison between before and after registration. (a) shows the fixed image (FRC) of subject H-1, (b) shows the moving image (TLC), (c) shows the deformed moving image (registration result), (d) shows the absolute difference image between the fixed and moving image, and (e) shows the absolute difference image between the fixed image and deformed moving image. All images are taken in the coronal plane. 43

4.2 Landmark error before registration showing standard deviation (unit : mm). 47

4.3 Landmark error after registration showing standard deviation for the three different cost functions (unit : mm). 47

4.4 Fissure alignment differences between the SSVMD and the sheet-likeness in H-1. (a) shows the fused image between the segmented FRC image (red color based) and the deformed segmented TLC image by using the combination of the SSTVD and SSVMD (green color based), (b) shows the fused image between the segmented FRC image (red color based) and the deformed segmented TLC image by using the combination of the SSTVD and sheet-likeness (green color based), and (c) shows the fused image between the deformed TLC (moving) image between the combination of the SSTVD and SSVMD (green color) and the combination of the SSTVD and sheet-likeness. All images are taken in the transverse plane. 50

A.1 Subject H-1. Comparison between before and after registration with three different cost functions. 53

A.2 Subject H-2. Comparison between before and after registration with three different cost functions. 54

A.3 Subject H-3. Comparison between before and after registration with three different cost functions. 55

A.4 Subject H-4. Comparison between before and after registration with three different cost functions. 56

A.5 Subject H-5. Comparison between before and after registration with three different cost functions. 57

A.6 Subject H-6. Comparison between before and after registration with three different cost functions. 58

B.1 Subject H-1. Box plot of the landmark error after registration with three different cost functions. 59

B.2 Subject H-2. Box plot of the landmark error after registration with three different cost functions. 60

B.3 Subject H-3. Box plot of the landmark error after registration with three different cost functions. 61

B.4 Subject H-4. Box plot of the landmark error after registration with three different cost functions. 62

B.5 Subject H-5. Box plot of the landmark error after registration with three different cost functions. 63

B.6 Subject H-6. Box plot of the landmark error after registration with three different cost functions. 64

CHAPTER 1
INTRODUCTION

1.1 Motivation

The lung is one of the most important organs in the human body. The main function of the lung is to perform the gas exchange component of the respiratory cycle. During the respiratory cycle, oxygen is inhaled into the lung and then carbon dioxide is exhaled to the air. Inhaled oxygen is diffused into the blood though an air sac called the aveoli. By this process, the lung provides fresh oxygen to the blood [1].

To understand how a lung works, it is necessary to understand the human anatomy. The basic structures of the lung are the airway and vessel trees, lung parenchyma, lobes, and fissures [2]. Specifically, normal human lungs consist of five different lobes which are divided by fissures, and lobes are connected by airway branches. There are the upper and lower lobes in the left lung and the upper, middle, and lower lobes in the right lung. This asymmetrical distribution of the lobes is caused by the location of the heart in the left side of chest [2].

During the respiratory process, when the lung volume changes, the amount the lung tissue expands depends on region of the lung. Lung volume change is caused by contraction and relaxation of the diaphragm, a muscle below the lung. Because of the location of the diaphragm, when the lung expands, there is more strain on the lowest part of the lung [1].

Lung image registration is a useful image processing technique to help under-

stand how the lung changes its shape/volume during the respiration process or for longitudinal study of the lung function analysis. Understanding these volume changes is an important issue pertaining to human physiology because many lung diseases, such as emphysema, asthma, and cystic fibrosis, are correlated with the lung volume changes during the respiration cycle [2].

There are many studies which try to improve the lung image registration accuracy [3–15]. They register inter-modality images to analyze longitudinal, and inter-phase changes at different inspiration or expiration pressures. There have been many attempts to improve the lung image registration accuracy by using various algorithms. Most lung image registration studies mainly focus on information of the image intensities as a cost function, such as the sum of squared differences, correlation coefficient, and/or mutual information [16].

Since the lung changes its density during the respiratory cycle, there are intensity differences in the computed tomography (CT) images between inspiration and expiration [12]. Due to these intensity differences, there is a limitation on the intensity based image registration algorithm. To overcome this limitation, some studies introduce alternative methods. Yin et al. introduce a new similarity measurement metric which uses the tissue volume differences of the lung CT image, and they show they can achieve reduced registration errors [9]. In addition, Cao et al. introduced a new lung specific registration algorithm, which is based on the vesselness information of the lung, and they demonstrate they can achieve improved vessel matching [7, 8]. Similarly, we think it would be possible to improve the registration accuracy by adding

incorporative anatomical structures of the lung, such as fissures and lobes.

1.2 Organization of the thesis

Chapter 2 discusses the background and related work. First, the image registration and similarity measurement functions (cost function) are described. This chapter describes the basics of image registration in the perspective of the transformation and corresponding features. This chapter also presents the currently published cost functions of the lung image registration. In addition to the background, previous lung image registration studies are described.

Chapter 3 presents the the proposed methods in detail. This chapter describes the overall registration process we would like to propose, and introduces the proposed additional cost function. The registration accuracy assessment is also described.

Chapter 4 discusses the experimental results of the proposed method. And Chapter 5 summarizes and concludes this thesis work.

CHAPTER 2
BACKGROUND AND RELATED WORK

2.1 Background

2.1.1 Image Registration

Image registration transforms one image (moving) to match another image (fixed/target). The two images can be taken at different times, have different fields of view, and/or be acquired using different modalities. In the medical imaging field, image registration helps find changes after clinical treatment, plan radiation therapy, and evaluate the treatment results. In addition, image registration can be applied to align different modalities between the functional images, such as positron emission tomography (PET), single photon emission computed tomography (SPECT), and anatomical images, such as CT and magnetic resonance imaging (MRI). By registering different modalities, we can see the subjects' anatomical structures and organ function overlaid together. This may have benefits to the relationship between the function and spatial location of the tissues [17].

The registration transformation can be subdivided to two different methods in the perspective of geometrical transformations: rigid and non-rigid [16]. The rigid transformation consists of a rotation, translation, and reflection. The main characteristic of the rigid transformation is preservation of the original size and shape during the transformation [16]. The rigid transformation can be used to align initial displacements, such as translation or rotation, of the lung. The non-rigid transfor-

mation is more suitable to register lung tissues because the lung volume changes are non-linear, and the amounts of the changes vary by the location of the lung. The non-rigid transformation does not preserve the original image size or shape. There are many non-rigid transformation methods: scaling, affine, projective, perspective, and curved [16].

There are three popular registration methods which are categorized by corresponding features to calculate or optimize the registration transformation: a point-based method, surface-based method, and intensity-based method.

2.1.1.1 Point-based method

The point-based method uses corresponding points, which are matching feature points between images, to calculate the transformation. Anatomical landmarks, such as bifurcation points (branch points) or salient points of the organs, are considered as corresponding points. The main advantage of the point based registration is its fast calculation speed because it is possible to solve the relation of points as simple linear algebraic equations [16].

2.1.1.2 Surface-based method

The surface-based method is widely used in the rigid registration protocol. This method calculates the transformation by minimizing the error of corresponding points between the moving and the fixed image surface [16]. It is possible to use landmark errors as a similarity measurement function by using an iterative closest points (ICP) or trimmed iterative closest points (TICP) algorithm [18]. The ICP/TICP

method consists of two steps, first, it is necessary to find closest pair points. The second step is to calculate the deformation fields which minimize the sum of the distance of paired points until it converges or reaches a pre-defined iteration number.

2.1.1.3 Intensity-based method

The intensity-based method uses the intensity values between the fixed and moving image. An intensity based registration minimizes differences between two images' picture element (pixel) or volume element (voxel) intensities [16]. To minimize the differences between two images, in other words, to maximize two images' similarity, a similarity function should be used. There are many studies demonstrating how to measure the similarity in the lung CT image registration [3–15]. There are three widely used intensity-based similarity measurement functions, which are the sum of squared differences (SSD), correlation coefficient (CC), and mutual information (MI) methods [16].

2.1.2 Similarity measurement

The similarity measurement function between the fixed and moving image is required to calculate transformation. The similarity function, which is also called correspondence cost function, depends on corresponding features [16].

2.1.2.1 Feature (point and/or surface)-based similarity function

A point-based method uses fiducial points to calculate the registration. We can calculate the fiducial registration error (FRE) [16] which is defined as

$$FRE_i = h(x_i) - y_i \tag{2.1}$$

where $h()$ denotes transformation, x_i and y_i denote feature points in the moving and target image, respectively, and i denotes i-th corresponding points. FRE_i is the distance differences between two corresponding points. The similarity function C for the point based registration can be the sum of squared distance differences for the feature points and/or normalized sum of squared distance differences.

$$C = \frac{1}{N}\sum_{i=1}^{N}|FRE_i|^2 \tag{2.2}$$

where N is the number of corresponding points.

2.1.2.2 Intensity-based similarity function

There are three widely used intensity-based similarity measurement functions, which are the sum of squared differences (SSD), correlation coefficient (CC), and mutual information (MI) methods. First, the SSD uses the intensity differences between the moving and target images. The SSD is widely used as a similarity function for the intensity based registration. The SSD can be easily calculated. The SSD value would be zero if two images match perfectly, but this may not be true in the lung CT image registration because the image voxels at the end of expiration (EE) and end of inspiration (EI) of the lung may have different intensities [9]. Because of the intensity differences between EE and EI, the SSD may require an additional intensity normalization scheme, such as histogram matching [19]. The SSD has a reasonable

reliability and fast computational speed. However, if two images have large intensity differences or severe noise in some regions, the registration result can be poor [20]. The formula for the sum of squared differences is defined as

$$SSD = \sum_{i=1}^{N} \{T(\boldsymbol{x}_i) - M(h(\boldsymbol{x}_i))\}^2 \tag{2.3}$$

where N is number of voxels of the overlapping regions [16]. From formula (2.3), T and M denote the target and the moving image intensity value at position $\boldsymbol{x}_i = (x_i, y_i, z_i)$, and $h()$ denotes transformation of the registration.

The correlation coefficient (CC) method shows the linear relationship between two images. The CC method can be used as a cost function in lung image registration. If the moving image is registered perfectly to the fixed image, the value of the CC should be one [16]. However, in lung image registration, the CC value may not be one due to the intensity differences between the EE and EI images. Therefore, the optimization process tries to maximize the CC value. Although the CC can be applied when complex transformation is necessary, the computational complexity will be increased. This increased computational complexity increases the calculation time and it is difficult to calculate the correct transformation matrix. In addition, the registration result might be poor if the voxels of two images have a non-linear relationship. The registration result may not match if there are outliers [21]. The calculation method of CC is shown below [16].

$$CC = \frac{\sum_i^N \{T(\boldsymbol{x}_i) - ave(T)\} \times \{M(h(\boldsymbol{x}_i)) - ave(M')\}}{\sqrt{\sum_i^N \{T(\boldsymbol{x}_i) - ave(T)\}^2 \times \{M(h(\boldsymbol{x}_i)) - ave(M')\}^2}} \tag{2.4}$$

From formula (2.4), $ave()$ denotes average or mean intensity of the image, $h()$ denotes transformation of the registration, T denotes the target image intensity value at position $\boldsymbol{x}_i$, and M' denotes the transformed moving image intensity value at position $\boldsymbol{x}_i$.

The mutual information method uses the joint entropy of two images. The joint entropy represents uncertainty between two or more variables. The joint entropy between two images may not be a proper similarity measurement function because the joint entropy is influenced by the overlaid regions of two images [16]. In addition, the MI may not be suitable for the same modality lung image registration because the image intensities (HU) vary by the amount of air in the lung. In addition, there is no information about the relationship between neighboring voxels. However, the MI method tries to minimize joint entropy and reduce the calculation complexity. To find the transformation, it is necessary to maximize the MI between the two images. The MI can be calculated by the two images' joint entropies [16, 22]. The formula for the probability distribution function (PDF) is defined as

$$PDF(i) = \frac{HIST(i)}{\sum_i HIST(i)} \tag{2.5}$$

for $i \in [1, \ldots, N]$, and $HIST(i)$ denotes image histogram at position i. The marginal entropy (ME) is defined as

$$ME(T) = \sum_{i \in T} \{PDF(i) \times \log\left(PDF(i)\right)\} \tag{2.6}$$

and

$$ME(M') = \sum_{j \in M'} \{PDF(j) \times \log\left(PDF(j)\right)\} \tag{2.7}$$

The joint entropy (JE) is defined as

$$JE(T, M') = -\sum_{j \in M'} \sum_{i \in T} \{PDF(i,j) \times \log\left(PDF(i,j)\right)\} \tag{2.8}$$

The MI is defined as

$$MI(T, M') = ME(T) + ME(M') - JE(T, M') \tag{2.9}$$

where T denotes the target image, and M' denotes the deformed moving image. The MI method is based on the joint histogram of the probability distribution function. The main advantage of the MI is that it is suitable for inter-modality registration. In addition, the MI results can be better when compared to the marginal entropy-based method since the marginal entropy is computed by separate entropies of two images. However, if the two images have large differences, it is possible that the entropies could have a low value and therefore the registration can result in mismatched regions [23]. It is important to restrict the calculation window in the MI registration method.

To improve the performance of the MI method, Studholme et al. [22] introduced the Normalized Mutual Information (NMI) method. According to Studholme

et al. the normalization scheme has a strength in the size of the overlapping region problem. The size of the overlapping region problem is that the size of the overlaid region is changed when image registration transforms the images. This change can bring large mismatching errors. However, the NMI is less variant than the MI method. As a result of the invariant characteristic, the NMI provide more strength than the MI method. The formula for the NMI is shown below formula (2.10)

$$NMI(T, M') = \frac{ME(T) + ME(M')}{JE(T, M')} \tag{2.10}$$

By using NMI method, they could achieve more robust results than MI method.

2.1.2.3 Lung CT image oriented similarity function

In recent studies, there were a couple of similarity measurement methods for the lung registration, such as the sum of squared tissue volume difference (SSTVD) [9] and the sum of squared vessleness measure difference (SSVMD) [7,8]. These methods were invented for the lung similarity measurements, which give improved registration accuracy. More details about these methods are introduced in the related work section in Chapter 2.2.

2.1.3 Related work

A brief summary of previous lung image registration studies focusing on the cost function will be explained here. Many researchers have tried to find the optimal lung CT image registration method [3–15]. Many methods use intensity based registration and non-rigid transformation. In addition, some methods use both rigid and

non-rigid transformation to minimize the registration errors.

Staring et al. [3] used the normalized correlation coefficient (NCC) as a cost function to implement a fully automated intensity-based registration algorithm by using Elastix, which is a toolbox for image registration [24]. This method consists of three registration steps. The affine transformation was used for the initial alignment. The second step consists of non-rigid registration without masks. Segmented lung volumes are used as the masks. It has been shown that by applying lung masks to the beginning of the registration step, the masks negatively affected the lung boundary regions. The final step of the registration was non-rigid registration with masks. B-Splines transformation (more details are explained in Chapter 3) method was applied to deform a non-rigid transformation with multiple grids. To maximize the similarity between the moving and fixed images, the NCC is used as the similarity function. The NCC can be defined as

$$NCC = \frac{\sum_i^N \{T(\boldsymbol{x}_i) - ave(T)\} \times \{M(h(\boldsymbol{x}_i)) - ave(M')\}}{\sqrt{\sum_i^N \{T(\boldsymbol{x}_i) - ave(T)\}^2 \times \{M(h(\boldsymbol{x}_i)) - ave(M')\}^2}} \tag{2.11}$$

The total cost function C can be

$$C = NCC + \alpha R \tag{2.12}$$

where R denotes the regularization term (bending energy). This method has strength to match both features and boundaries. This strength comes from the boundary masked image. However, they exclude the regularization term because of the time

complexity and dependent parameter α. The entire process takes less than 17 minutes in general (the original image size is $512 \times 512 \times 579$ voxels) on an Intel Xeon W3520 @ 2.66 GHz, 4GB RAM, Windows 7 64 bit computer. However, this method has some limitations with regard to the singularities, which represent undesirable deformations, because of the removal of the regularization term.

Dougherty et al. [4] used sum of squared differences (SSD) to register CT lung volumes using an optical flow method. In this study, an optical flow is used as a motion estimation method. They use an optical flow method to estimate positional changes of two different volumes. To minimize differences between these, they use the SSD of the two images after Laplacian filtering to calculate motion parameters. The formula for this cost function $C(u)$ is shown below

$$C(u) = \sum_{x} \{L_i(x,t) - L_i[x + u(x), t+1]\}^2 \tag{2.13}$$

where x is position of the image, L_i denotes Laplacian filtered image intensity, i is image pyramid level, t and $t+1$ represent reference and moving image, and $u(x)$ is a motion parameter (pixel velocity) which minimizes the SSD of $L_i(t)$ and $L_i(t+1)$. In addition, the SSD is used as a similarity function to minimize differences between the moving image and the fixed image. The optical flow method has an advantage for the lung CT image registration because the CT image has high resolution and high contrast in the vessels, which can be used as landmarks. However, this method has weakness in the field of view (FOV) change and initial displacements. For example, the optical flow method cannot estimate or compensate for missing information when

there are large initial displacements or the lung nodule size changes.

Han [5] used hybrid cost function of the MI and the normalized SSD (NSSD). To select features, he uses robust 3D speed up robust feature (SURF) to register lung CT images. SURF is a feature detector and descriptor to help recognize features. Robust 3D SURF was used to extract feature points to calculate motion movements. The main disadvantage of the intensity-based registration is the high computational costs. To reduce computational costs, Han chose rigid registration prior to the non-rigid registration. In addition, the feature-constrained MI registration was applied. To find optimal transformation, Han uses a non-parametric model defind as

$$T(x) = x + U(x) \tag{2.14}$$

where T is a spatial transformation, U is a displacement field, and x is a position [25]. The cost function for feature-constrained MI registration is

$$C(T, M) = -MI(T, M') + \alpha R + \beta \sum_{i=1}^{N} \{T(\boldsymbol{x}_i) - M(h(\boldsymbol{x}_i))\}^2 \tag{2.15}$$

where N denotes the number of the overlaid voxels, α and β are weight factors, and R denotes the regularization term, which is Laplacian. After the feature-constrained MI registration, the MI and NSSD are applied as a final registration process. The intensity normalization scheme can be applied to the SSD method to reduce the intensity variation. The image intensity normalization scheme is defined as

$$\bar{T}(x) = \frac{T(x) - \mu_T(x)}{\sigma_T(x)} \tag{2.16}$$

for $\sigma_T = \sqrt{\{G_\sigma * (T - \mu_T)\}^2}$, and $\mu_T(x)$ is defined as

$$\mu_T(x) = G_\sigma * T(x) \tag{2.17}$$

for G_σ denotes Gaussian smoothing ($\sigma = 2$ voxels). NSSD is defined as

$$NSSD(T, M) = \frac{1}{N} \sum_{i=1}^{N} \left(\bar{T}(\boldsymbol{x}_i) - \bar{M}(h(\boldsymbol{x}_i)) \right)^2 \tag{2.18}$$

The final cost function for this method is

$$C(T, M) = -MI(T, M') + \alpha NSSD(T, M) \tag{2.19}$$

A feature based hybrid registration method may reduce calculation time because it calculates features' correspondence only. However, there is a possibility that these features may not represent the anatomical structures in the lung CT image. This misalignment or mismatch of features may bring an unpredictable registration result.

Kabus et al. [6] used the SSD as a similarity measurement method to calculate an elastic image registration with the combination of two different registration methods. The first method is the affine transform. This is useful to align initial displacements which are the differences between the first scan and follow-up scan. To avoid misalignments, lung masks are used to register the volumes. In addition to the affine transform, the second method is the elastic registration which minimizes both a similarity measurement and a regularizing term. In this registration algorithm, the SSD is used as a similarity measurement method. The Navier-Lamé equation, which is a linear elasticity measurement method, is used as an elastic regularization because

the lung CT image can be considered as an elastic material. The cost function C for this method is shown below (2.20)

$$C = SSD + \alpha R \tag{2.20}$$

$$SSD = \frac{1}{2}\int_{\Omega}\Big(T(\boldsymbol{x}) - M(h(\boldsymbol{x}))\Big)^2 dx \tag{2.21}$$

$$R = \int_{\Omega}\left(\frac{\mu}{4}\sum_{i,j=1}^{3}\Big(\partial_{x_j}u_i(x) + \partial_{x_i}u_j(x)\Big)^2 + \frac{\lambda}{2}(\nabla\cdot u(x))^2\right)dx \tag{2.22}$$

where Ω is a domain which is satisfied $\Omega \subset \mathbb{R}^3$ and deformation vector u deformed in $\mathbb{R}^3 \to \mathbb{R}^3$, R is an elastic regularization term, and λ and μ are Lame constants. This method suggests a fast registration method for entire lung CT images. It takes less than 30 minutes including the pre-/post-processing step in 512×512×579 (original size of image) using MATLAB on 2.83 GHz, 3 GB RAM. However, this method performs poorly if there is a large deformation, such as lower lung areas and fissures. Kabus et al. mentioned that the poor registration performance is no usage of fissure detection in the protocol. Although the regularizing term can help to reduce singularity errors, this regularizing term also can prevent deformation of the moving image.

Yin et al. [9] introduce an improved similarity measurement method which is the sum of squared tissue volume difference (SSTVD). The initial assumption of the SSTVD is that the CT image intensity consists of the tissue or air volume. As shown in formula (2.23), the CT intensity (Hounsfield Unit: HU) in position x can be calculated by the the tissue and air volume.

$$I(x) = \frac{(V_{air} \times HU_{air} + V_{tissue} \times HU_{tissue})}{V_{voxxel}} \tag{2.23}$$

As a result, it is possible to calculate the SSTVD. The tissue volume can be calculated as

$$Vol(x) = v(x) \times \frac{I(x) - HU_{air}}{HU_{tissue} - HU_{air}} \tag{2.24}$$

$Vol(x)$ is the volume of the voxel at position x, $I(x)$ is HU at position x. Yin et al. assume that HU in air is -1000, and HU in tissue is 55. With this assumption, they can measure the similarity as

$$SSTVD = \sum_{\boldsymbol{x} \in \Omega} \Big(V_T(\boldsymbol{x}) - V_M(h(\boldsymbol{x})) \Big)^2 \tag{2.25}$$

where Ω denotes overlap region of two images, V_T denotes the tissue volume of the target image, V_M denotes the tissue volume of the moving image, and $h()$ denotes the transformation matrix. To apply the transformation, cubic B-spline was used to deform the lung because of its performance and computational efficiency. With the SSTVD, Yin et al. show that the volume of local tissues are preserved more than the SSD. The advantage of this method is preserving the lung tissue volume and weight, and providing more deformation of the lung volume change. However, this method has limitations. If the data set has severe noise, minimizing the SSTVD errors may converge to the local minima. In addition, if the data sets have large initial displacements, the deformation of the registration can be mismatched. The reason is that B-Spline deformation depends on its grid size. Although the multi scale scheme

may help reduce registration errors and calculation time, the maximum displacement still depends on B-spline grid size. The reduced image resolution for a multi scale scheme can bring information loss, and this loss may affect to the registration result.

Cao et al. [7,8] introduce sum of squared vesselness measure difference (SSVMD) as a new similarity measurement method. This method uses a lung vessel structural shape and characteristics of the respiratory system. In the respiratory process, the lung vessel tree structures do not change their structure. Lung blood vessels can be used to help to improve the registration accuracy. To calculate vesselness of the lung, they used the eigenvalues of the Hessian matrix. The Hessian matrix is a second order partial differential matrix of the image. More details about the Hessian matrix is showed in Chapter 3. The vesselness measurement is computed from the Frangi's vesselness function V_f as

$$V_f(\lambda) = \begin{cases} \left(1 - e^{\frac{V_a{}^2}{2\alpha^2}}\right) \cdot \left(1 - e^{\frac{V_b{}^2}{2\beta^2}}\right) \cdot \left(1 - e^{\frac{V_c{}^2}{2\gamma^2}}\right) & \text{, if } \lambda_2 < 0 \text{ and } \lambda_3 < 0 \\ 0 & \text{, otherwise} \end{cases} \tag{2.26}$$

where $V_a = \frac{|\lambda_2|}{|\lambda_3|}$, $V_b = \frac{|\lambda_1|}{\sqrt{\lambda_2 \lambda_3}}$, $V_c = \sqrt{\lambda_1^2 + \lambda_2^2 + \lambda_3^2}$, $\lambda_1, \lambda_2, \lambda_3$ denotes eigenvalues of the Hessian matrix, and α, β, γ are thresholds for controlling the sensitivity of the vesselness measurement [26]. Cao et al. rescale the value of vessleness from 0 to 1, and a larger value means it has more vessel-like feature. By adding the SSVMD constraints to the SSTVD [9], MI and SSD, the SSVMD method with the weighted factor helps to achieve improved the registration accuracy, especially near the vessel areas. The cost function $SSVMD$ is defined as

$$\text{SSVMD} = \sum_{\boldsymbol{x}\in\Omega}\Big(V_{f-T}(\boldsymbol{x}) - V_{f-M}(h(\boldsymbol{x}))\Big)^2 \tag{2.27}$$

where Ω denotes overlap region of the images, V_{f-T}) denotes vesselness of the target image, V_{f-M} denotes vesselness of the moving image, and $h(\boldsymbol{x})$ denotes the transformation matrix. To transform the image, the authors use the uniform quadratic B-spline to transform the moving image with image pyramids, which is a multiresolution scheme. However, the grid size of the B-spline limits the maximum deformable size. If there is a large initial displacement between the two images, the registration transformation may not find exact deformation for the moving image to fit the fixed image. In addition, calculating the B-Spline transformation takes a long time as it requires solving the formulation for each control point. it is possible to mismatch the corresponding vesselness. This may bring some errors during the registration process.

Betke et al. [10] use the sum of squared residual errors to develop corresponding anatomical landmarks matching algorithm to register lung CT images. Their method is based on the landmark based registration algorithm with the sum of squared errors of the landmark distances. The cost function for sum of squared error C is defined as

$$C = \sum_{i=1}^{N}(x_i - h(p_i))^2 \tag{2.28}$$

where x_i is a series of points in the target image, and p_i is a series of corresponding points in the moving image, and $h(x)$ is the transformation which transforms corresponding points to target points. The first step of this method is to find corresponding points. To accomplish this, Betke et al. use a template matching algorithm to find the

center points of the trachea. With these points, they can calculate affine transform. To verify the registration accuracy, they test nodules within the lung. However, the all pair points are decided by Euclidean distances, and therefore the points might not be the same corresponding physical points between the two images. This error may bring errors to the registration precision. However, this method is based on global registration which is not suitable for lung CT image registration because the lung volume changes more at the base than the apex of the lung.

Busayarat and Zrimec [11] used landmark errors as a cost function to implement a ray-tracing based high resolution lung CT image registration. This is a hybrid registration method of a point based and a surface based registration. For the point based global registration, the hilum of the lung (lung root), sternum and spinal cord are used as landmark points to calculate rotation, translation, and scaling. The point based global registration was used to align initial displacements. For the surface detection, the adaptive thresholding and the active contour snakes [27] methods are used. The ray tracing method was used to find corresponding points between the two images. The lung roots, which are defined as the main branch points connected to the lung, are used as the origin points of the ray. By using the distance of the two rays from their respective origins, the desirable registered points are calculated. The main advantage of this method is that registered points are located inside of the lung boundaries. However, the major disadvantage of this method is that the internal registration results may be varied because this registration method is based on surface information. In other words, although to keep the singularities is an important issue

in the pulmonary registration, this method cannot guarantee the singularities in lung image registration [15].

Schmidt-Richberg et al. [12] presented a fully automated registration method with the mean squared differences of distance. There are two main processes in this algorithm. The first step is a pre-registration, which is performed by the surface point registration. The second step is an image-based diffeomorphic registration. To calculate the pre-registration transform, lung masks, marching cubes algorithm, iterative closest point (ICP) algorithm, and thin plate spline (TPS) interpolation methods are used. After the pre-registration process, they apply an image-based diffeomorphic registration. One of the strongest points in the diffeomorphic transformation is that object topology is preserved. This characteristic helps anatomically meaningful transformation. Diffeormorphic transformation is calculated by the solution of the stationary flow equation. In the diffeormorphic registration process, the mean squared difference (MSD) of landmarks is used to stop the registration process by updating the terms of the velocity field and performing a diffusive regularization. The landmark points are extracted by using the automatic landmark detection algorithm where used [28]. However, due to the intensity differences at the different respiratory cycles, it is necessary to do histogram matching between the moving and fixed images before the registration process. The desirable cost function for this registration method is finding the velocity field $\boldsymbol{v}$ which minimizes the distance D between of the target and moving image with regularization term R. This can be expressed as

$$C[exp(\boldsymbol{v})] = D[T, M; exp(\boldsymbol{v})] + \alpha R[exp(\boldsymbol{v})] \tag{2.29}$$

where T denotes target image, M denotes moving image, $R[exp(\boldsymbol{v})] = \int_\Omega ||\nabla \boldsymbol{v}||^2 \, dx$, and $exp()$ denotes the group exponential map. This method has many advantages, such as preventing singularities, ease of calculating the inverse of the transform, and reducing calculation time and memory usages. However, it is possible that the deformation can cause singularities during the pre-registration step.

Muenzing et al. [13] introduce a novel local regularization of image registration by using a diffeomorphic demon algorithm using the SSD and boundary distances. By using a machine learning process, the local regularization is considered as a regression problem. In this paper, they focuse on the diffusion-like kernel as a regularization term. By optimizing parameters of the regularizers, they test for the best combination of the kernel. They apply the diffeomorphic demons algorithm which is proposed by Vercauteren et al. [29] to represent their non-parametric registration algorithm. In their study, a moving image which consists of a deformable grid is diffused through the boundary of the fixed image. This diffusing direction and gradient are calculated by a vector field (e.g. optical flow). The cost function proposed by Vercauteren et al. [29] is

$$C(v,t) = \frac{1}{{\sigma_n}^2} \cdot \frac{1}{2\Omega} \sum_{\boldsymbol{x} \in \Omega} |T(\boldsymbol{x}) - M(h(\boldsymbol{x}))|^2 + \frac{1}{{\sigma_u}^2} D(t,v)^2 + \frac{1}{{\sigma_r}^2} R(t) \tag{2.30}$$

where v denotes a vector field which is a point correspondence between image pixels, t denotes a transformation model, T and M denote the image intensity of fixed and

moving images at position $\boldsymbol{x}$, D denotes distance, R denotes a regularization term, ${\sigma_n}^2$ = noise, ${\sigma_u}^2$ = spatial uncertainty on the correspondences, and ${\sigma_r}^2$ = the amount of regularization. To optimize the transformation, they use a combination of the lung boundary region and lung tissues with the landmark-based optimization method. However, since these local regularizers are not related with anatomical structures, it is possible that the deformation results transformed in undesirable directions. To avoid this problem, they add the signed Euclidean distance transformation based on the vessel segmentation. Additionally, to combine the regularization analysis and anatomical information, Muenzing et al. may achieve better results in registration. However, this algorithm has a weakness when the volume change of data pairs is greater than the volume change of trained data sets. The registration results may be undesirable. This is because the registration calculation is based on the trained data sets, and these trained data sets work as a regularization term of the transformation.

Modat et al. [14] introduce a combination of the local and global registration method called NiftyReg using the CC and NMI methods. They use a block-matching algorithm for the global registration of the feature alignments, and the Free-Form Deformation (FFD) algorithm using the B-Spline interpolation scheme for the local registration. A graphic processor unit is also used to reduce calculation time. For the global registration using the block-matching algorithm, it is necessary to divide the fixed image and the moving image into blocks or sub-volumes. To find similarities between the two images, they use a least trimmed squares method via the cross correlation coefficient because this method has an advantage in reducing outliers. They

consider 50% of correspondences as inliers and the other 50% as outliers because the blocks may not be comparable [30]. The formula for the cross-correlation coefficient for the block matching algorithm is

$$CC(B_{xy}, B'_{uv}) = \frac{1}{N^2} \sum_{i=0}^{N-1} \sum_{j=0}^{N-1} \left(\frac{\left[M'(x+i, y+j) - \bar{M'}_{(x,y)}\right] \times \left[T(u+i, v+j) - \bar{T}_{(u,v)}\right]}{\sigma_{M'}(x,y) \cdot \sigma_T(u,v)} \right) \tag{2.31}$$

where B denotes a block of the image, σ denotes the standard deviation of the block, $\bar{M'}$ and $\bar{T}$ denotes the mean of the block [30]. After the calculation of the correspondence of each block, a global transformation is applied. In addition to the global registration scheme, for the local registration, they apply the FFD to deform the images. This registration algorithm includes the normalized mutual information (NMI) and bending energy. The NMI is used as a similarity measurement, and the bending energy as a deformation constraint. They define the bending energy as the sum of squared second derivatives of the transformation. In addition, the squared Jacobian determinant is used to ensure singularity. The cost function of this method is

$$\begin{aligned} C(F, M') &= (\alpha - \beta) \left(\frac{ME(T) + ME(M')}{JE(T, M')} \right) \\ &\quad - \alpha \sum_{xin\Omega} \left[\left(\frac{\partial^2 h(x)}{\partial x^2} \right) + \left(\frac{\partial^2 h(x)}{\partial y^2} \right) + \left(\frac{\partial^2 h(x)}{\partial z^2} \right) \right] \\ &\quad - \alpha \sum_{xin\Omega} \left[2 \times \left(\frac{\partial^2 h(x)}{\partial xy} \right) + \left(\frac{\partial^2 h(x)}{\partial yz} \right) + \left(\frac{\partial^2 h(x)}{\partial xz} \right) \right] \\ &\quad - \beta \times \sum_{xin\Omega} \log \left(|\mathbf{Jac}(h(x))| \right)^2 \end{aligned} \tag{2.32}$$

where $\alpha and \beta$ denote user defined weights, $ME(T)$ and $ME(M)$ denote the marginal entropy, $JE(T, M)$ denotes the joint entropy, $h(x)$ denotes transformation, **Jac** de-

notes the Jacobian determinant at position x. The main strengths of this algorithm are calculation speed and matching of the lung boundaries. However, there are some mis-matched points in the registration process, especially in near fissure areas and the lower part of the lungs. This means if there are large displacements or intensity changes, this method cannot compensate for these large differences.

CHAPTER 3
METHODS

3.1 Data acquisition

Six normal human data sets are used for this thesis. For each subject, a pair of volumetric CT images are acquired from Siemens Sensation 64 multi-detector CT scanner in supine position. Each subject is named from H-1 to H-6. Each pair consists of two different volumes. One is functional residual capacity (FRC), and the other is total lung capacity (TLC). These are acquired in breath-holding status. Six pairs of CT image data sets are acquired. These twelve images consist of $0.5 \sim 0.6$mm sectional pixel spacing and 512×512 matrix. The spatial resolution of the in-plane is approximately 0.6×0.6mm. Figure 3.1 shows an example of the subject H-1.

3.2 Overall process

Figure 3.2 shows a block diagram of the entire procedure. Six human data sets are used to verify registration accuracy. For this study, we use total lung capacity and functional residual capacity images. Total lung capacity (TLC) is the volume in the lung at maximal inspiration. TLC is the sum of vital capacity and residual volume. Vital capacity is the volume of air exhaled after maximal inhalation. Residual volume is the volume of air remaining in the lung after maximal exhalation. Functional residual capacity (FRC) is the volume in the lung at the end of expiration. All the experiments are applied from TLC to FRC image registration.

In this registration process, to transform one image to another, the cubic B-

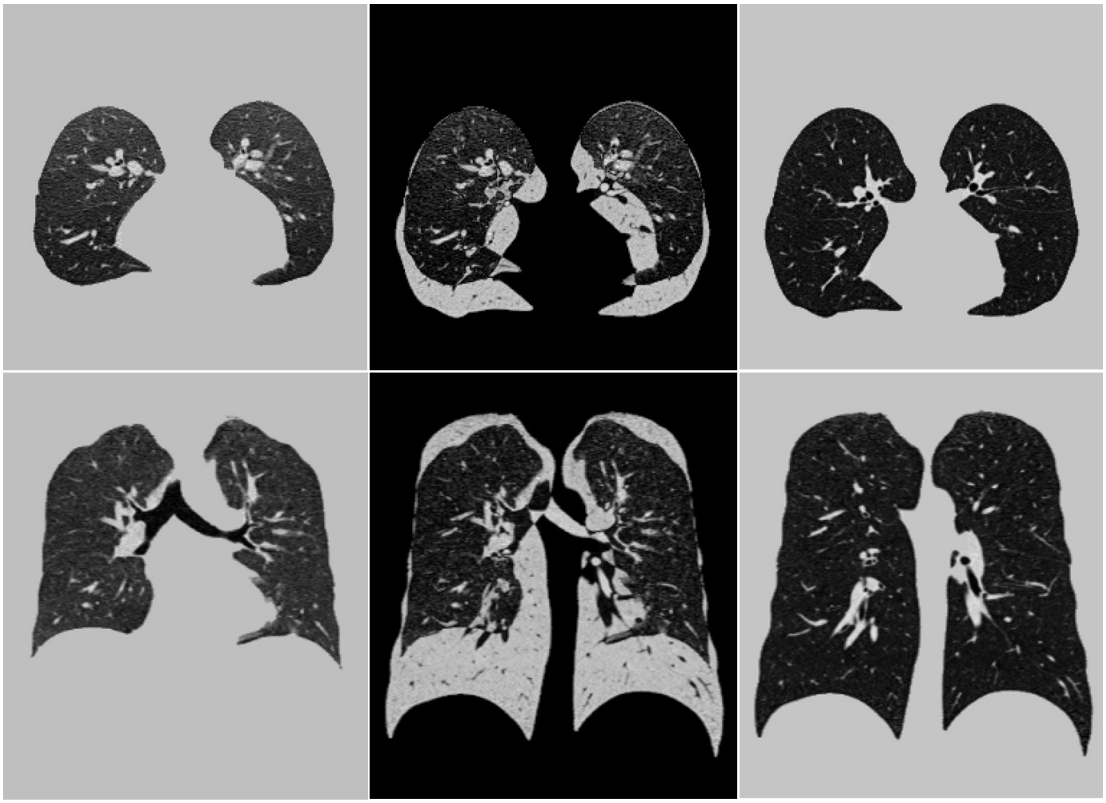

Figure 3.1: Segmented FRC and TLC lung images of the H-1 data set. The upper row shows the transverse plane, and the lower row shows the coronal plane. (a) shows FRC image, (b) shows the absolute difference image between FRC and TLC image, and (c) shows TLC image

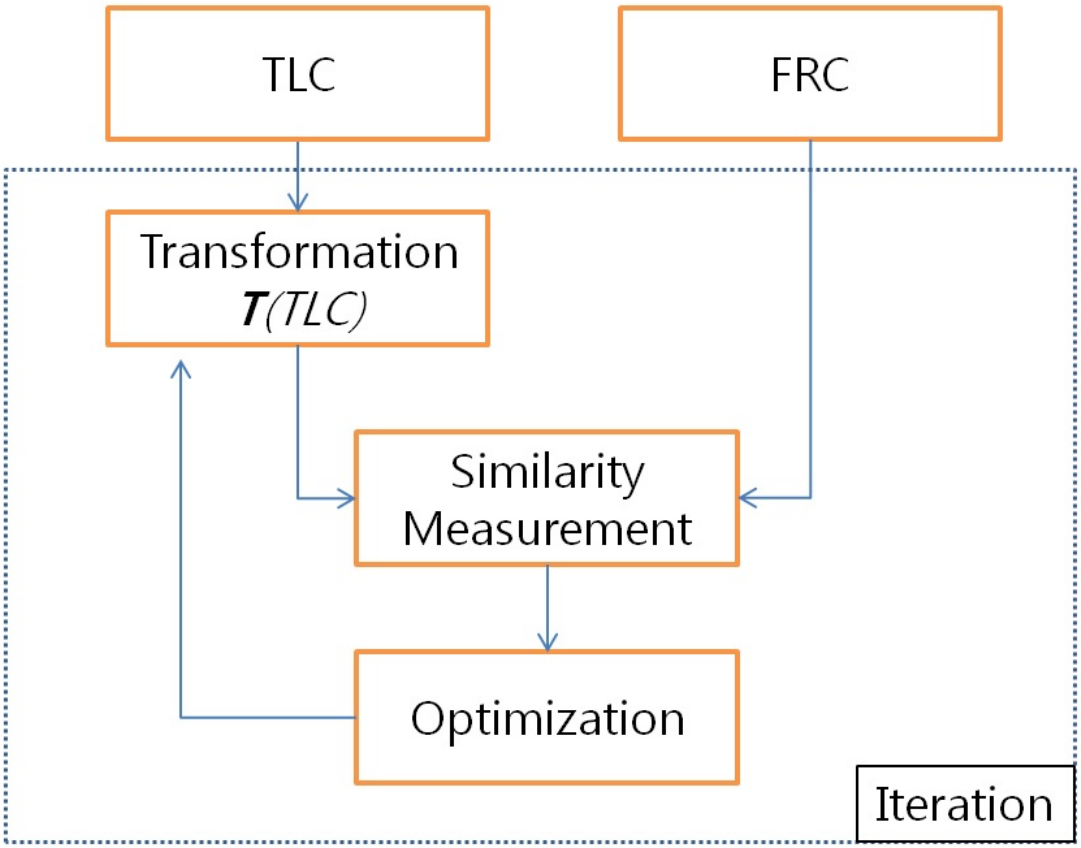

Figure 3.2: The entire procedure of the registration

Spline transformation is used. The B-Spline transformation is widely used in non-rigid medical image registration [31]. $t(\mathbf{x})$ is transformation model which deforms every point in one image to its corresponding point.

$$t(\mathbf{x}) = \mathbf{x} + \sum_{i \in S} \omega_i \cdot \boldsymbol{\beta}(\mathbf{x} - \mathbf{x}_i) \tag{3.1}$$

where $\mathbf{x}$ denotes vector $(x, y, z)^T$, S denotes spline grid, ω_i denotes the coefficient of the i-th control point, and $\boldsymbol{\beta}(\mathbf{x})$ denotes a separable convolution kernel which can be defined as

$$\boldsymbol{\beta}(\mathbf{x}) = \boldsymbol{\beta}(x)\boldsymbol{\beta}(y)\boldsymbol{\beta}(z) \tag{3.2}$$

The uniform cubic B-Spline basis function can be defined as

$$\boldsymbol{\beta}(x) = \begin{cases} (x^3 + 6x^2 + 12x + 8)/6 & , -2 < x \leq -1 \\ (-3x^3 - 6x^2 + 4)/6 & , -1 < x \leq 0 \\ (3x^3 + 6x^2 + 4)/6 & , 0 \leq x < 1 \\ (-x^3 + 6x^2 - 12x + 8)/6 & , 1 \leq x < 2 \\ 0 & , \text{otherwise} \end{cases} \tag{3.3}$$

A multiresolution scheme is used in order to increase the calculation speed and registration accuracy. The basic idea of the multiresolution scheme is that, in lower resolution, the registration tries to match an initial alignment of the two images, and gives the transformation information to the next step until the registration process reaches final resolution. This multiresolution scheme helps avoid local optima at lower scales and improve matching at the final resolution. We use this multiresolution

process starting from one-eighth and increasing by a factor of two until full resolution is reached. Table 3.1 shows how the multiresolution strategy is applied.

Table 3.1: Applied multiresolution scheme

Image resolution	B-Spline grid size	Max iteration
1/16	256mm	4000
1/8	128mm → 64mm	4000
1/4	32mm → 16mm	400
1/2	16mm → 8mm	200
1	8mm → 4mm	50

3.3 Anatomical similarity function

The similarity function measures how the moving image matches to the target image with a given transformation. As mentioned in Chapter 2, there are many similarity functions. We choose to use the SSTVD as a main cost function because this similarity measurement gives better registration accuracy than the SSD [9]. In addition to the SSTVD, we design the lung specific cost function which uses the fissure-likeness measurement. Incorporating fissure and lobe information can improve registration accuracy because of these features' physiological characteristics. The human lungs (left and right sides) are composed of five different lobes, two left lobes and three right lobes. These lobes are divided by fissures. Lower lobes expand more than upper lobes when the main expansion forces come from the contraction of the diaphragm muscles. Since the lung deformation during the respiratory cycle is a

non-homogeneous process, the location of fissures is important to assess registration accuracy. Since the shape of fissures seems to have a sheet-like structure, fissures can be highlighted as a sheet-like structure. For this reason, fissures are added to improve registration accuracy. Before we start to explain about fissure-likeness, it is necessary to understand the background of the Hessian matrix based shape detection method.

The Hessian matrix is composed of second order partial derivatives, and is defined as

$$H(\mathbf{f}) = \begin{bmatrix} \frac{\partial^2 \mathbf{f}}{\partial {x_1}^2} & \frac{\partial^2 \mathbf{f}}{\partial x_1 \partial x_2} & \frac{\partial^2 \mathbf{f}}{\partial x_1 \partial x_3} \\ \frac{\partial^2 \mathbf{f}}{\partial x_2 \partial x_1} & \frac{\partial^2 \mathbf{f}}{\partial {x_2}^2} & \frac{\partial^2 \mathbf{f}}{\partial x_2 \partial x_3} \\ \frac{\partial^2 \mathbf{f}}{\partial x_3 \partial x_1} & \frac{\partial^2 \mathbf{f}}{\partial x_3 \partial x_2} & \frac{\partial^2 \mathbf{f}}{\partial {x_3}^2} \end{bmatrix} \tag{3.4}$$

where $\mathbf{f}$ is a intensity value function which consists of (x_1, x_2, x_3) which represent each axis. Eigenvalues of the Hessian matrix can be calculated by $det(H(\mathbf{f}) - \boldsymbol{\lambda} I) = 0$ where $\boldsymbol{\lambda}$ denotes eigenvalues $\boldsymbol{\lambda} = (\lambda_1, \lambda_2, \lambda_3)$ in the given matrix $H(\mathbf{f})$, and I is the identity matrix. Eigenvalues represent the length of corresponding eigenvectors, and eigenvectors ($\boldsymbol{v}$) have the same direction as $H(\mathbf{f})\boldsymbol{v}$. Eigenvectors can be calculated as $H(\mathbf{f})\boldsymbol{v} = \boldsymbol{\lambda}\boldsymbol{v}$ where $\boldsymbol{v}$ is eigenvectors which can be represented as a 3×3 matrix. Sato et al. introduce a tissue classification measurement method based on local intensity structure of the image [32]. Figure 3.3 shows how the tissue structure is classified.

The sheet-likeness measurement can be defined as the extension of Frangi's objectness function [26, 33].

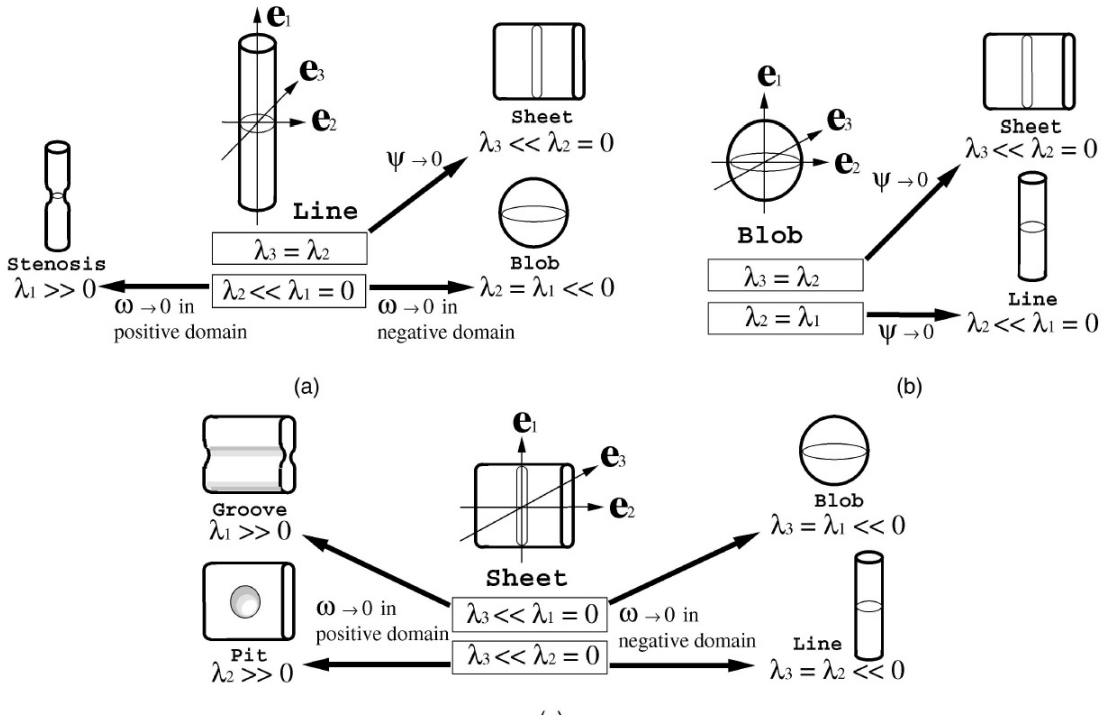

Figure 3.3: Tissue shape classification measure based on eigenvalues of the image. (a) Line measure. (b) Blob measure. (c) Sheet measure. In this figure, $\lambda_1 \geq \lambda_2 \geq \lambda_3$. Figure from Sato et al. [32].

$$F(\lambda) = \begin{cases} \left(1 - e^{\frac{{V_a}^2}{2\alpha^2}}\right) \cdot \left(1 - e^{\frac{{V_b}^2}{2\beta^2}}\right) \cdot \left(1 - e^{\frac{{V_c}^2}{2\gamma^2}}\right) & \text{, if } \lambda_2 < 0 \text{ and } \lambda_3 < 0 \\ 0 & \text{, otherwise} \end{cases} \tag{3.5}$$

$${V_a}^2 = \frac{\prod_{i=T+1}^{N} |\lambda_i|}{\prod_{i=T+2}^{N} |\lambda_i|^{\frac{N-T}{N-T-1}}} \tag{3.6}$$

$${V_b}^2 = \frac{\prod_{i=T}^{N} |\lambda_i|}{\prod_{i=T+1}^{N} |\lambda_i|^{\frac{N-T+1}{N-T}}} \tag{3.7}$$

$${V_c}^2 = \sqrt{\sum_{i}^{N} {\lambda_i}^2} \tag{3.8}$$

where λ_i denotes eigenvalues of the Hessian matrix ($|\lambda_i| \leq |\lambda_{i+1}|$), N is a dimension of the image, T is dimension of the structures which is defined as 0 for blobs, 1 for vessels, 2 for plates, and 3 for hyper-plates ($T < N$), and α, β, and γ are thresholds for controlling the sensitivity of the vesselness measurement [26]. In this thesis, we use $N = 3$, $T = 2$, $\alpha = \beta = 0.5$ and $\gamma = 5$. V_a is used to distinguish plate-like and line-like structures. V_b accounts for a blob-like structure. V_b has a maximum value for a blob-like structure and zero when $\lambda_1 \approx 0$, or λ_2 has a very small value. V_c is the norm of eigenvalues, and V_c has a lower value when it is in the background and has low contrast.

Table 3.2: Object patterns decided by eigenvalues.

Singular			Plural
λ_1	λ_2	λ_3	
Low	Low	High	Plate-like structure
Low	High	High	Tube-like structure
High	High	High	Blob-like structure

Table 3.2 adapted from Frangi et al. [26] shows the object shapes which are decided by eigenvalues. When eigenvalues consist of $\lambda_1 \approx \lambda_2 \lll \lambda_3$, this object can be classified as a plate-like structure. If eigenvalues have $\lambda_1 \lll \lambda_1 \approx \lambda_3$, this object has a tube-like structure. In addition, a blob-like structure has eigenvalues $\lambda_1 \approx \lambda_2 \approx \lambda_3 \ggg 0$. The multiresolution scheme is applied to increase the sensitivity of the shape structure. Gaussian smoothing is used to apply the multiresolution strategy. Maximum values are selected at each resolution.

More information is observed in the sheet-likeness measurement than the vesselness measurement. Figure 3.4 shows the extracted vesselness measurement results and comparison between the extracted vesselness and sheet-likeness image. The major difference is the existence of the fissures. The red circle points out the location of the fissures. Fissures mainly consist of green color which means that the vesselness method cannot detect fissures.

Figure 3.5 and 3.6 show extracted sheet-likeness structures of subject H-1. There are many vessel walls also extracted because of the Hessian matrix kernel size. At first, we thought vessel walls should be removed because we would like to focus

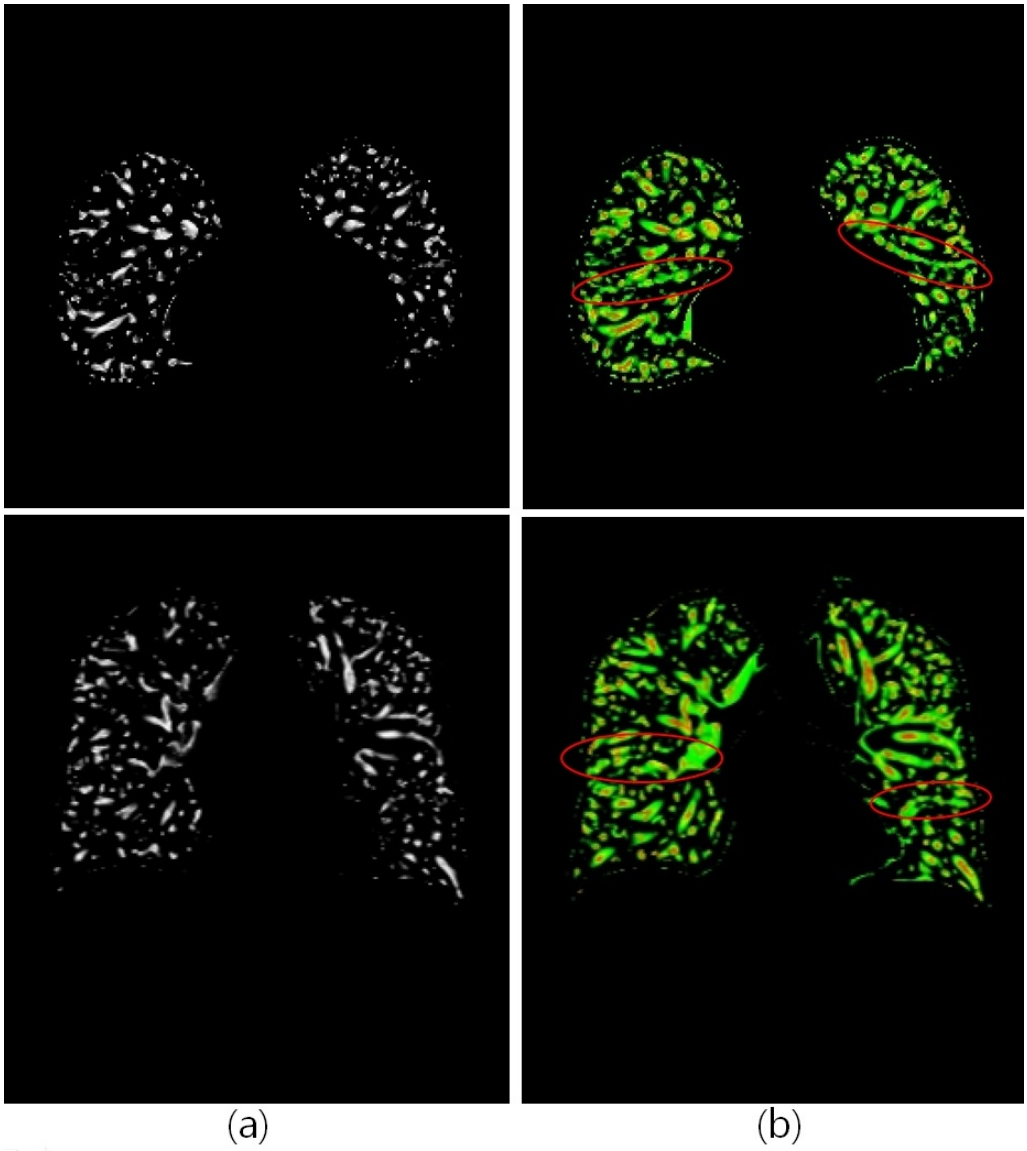

Figure 3.4: Comparison between vesselness and sheet-likeness. The upper row represents the transverse plane, and the lower row represent the coronal plane, (a) shows the vesselness results, (b) shows the fused image between vesselness and sheet-likeness. Red color is used for vesselness, and green color is used for sheet-likeness. Red circles represent the location of the fissures.

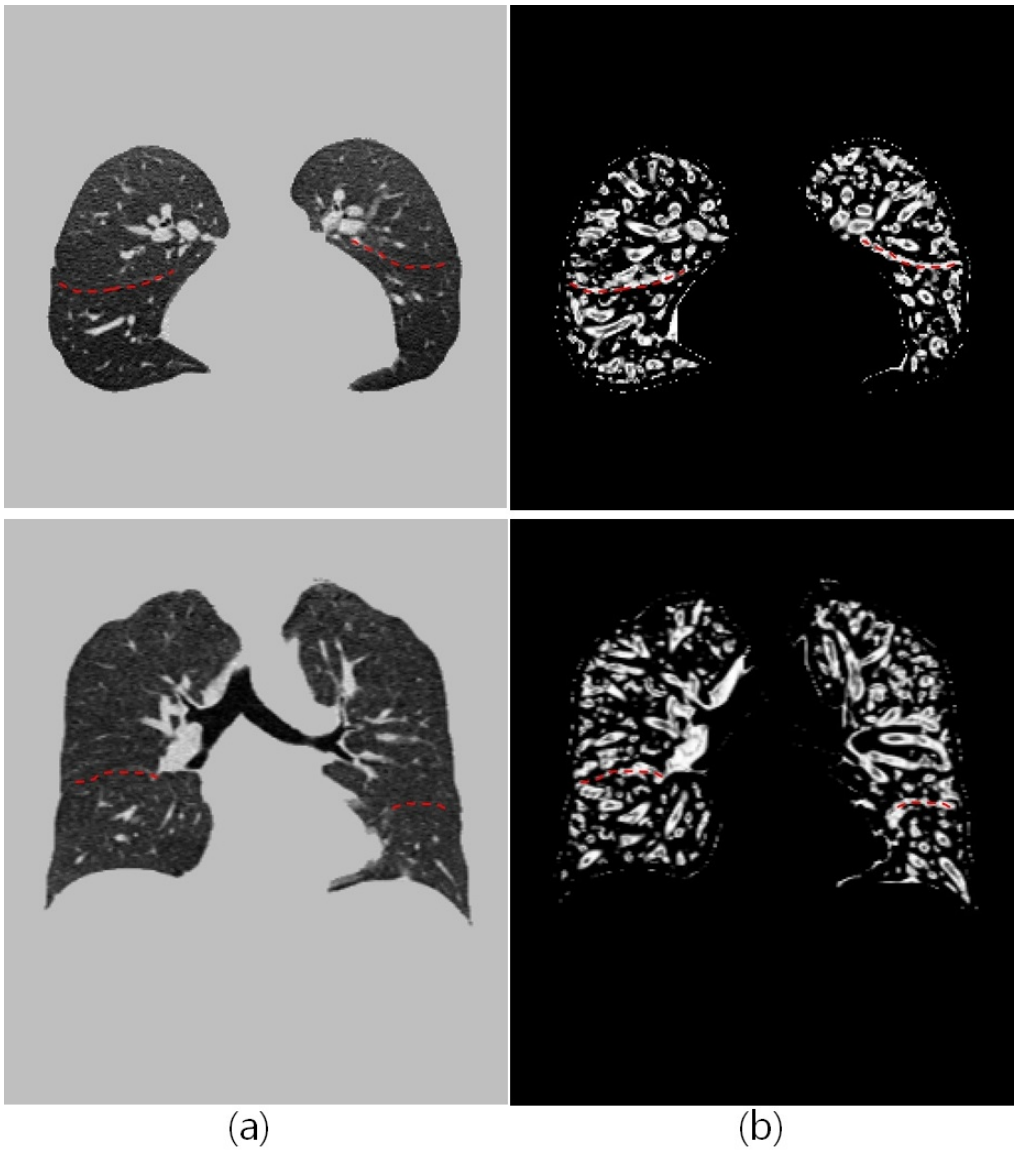

Figure 3.5: Extracted fissure-like structure in FRC. The upper row shows the transverse plane, and the lower row shows the coronal plane, (a) shows the corresponding CT image, and (b) shows the extracted fissure-like structure. The red dotted line represents the location of the fissure.

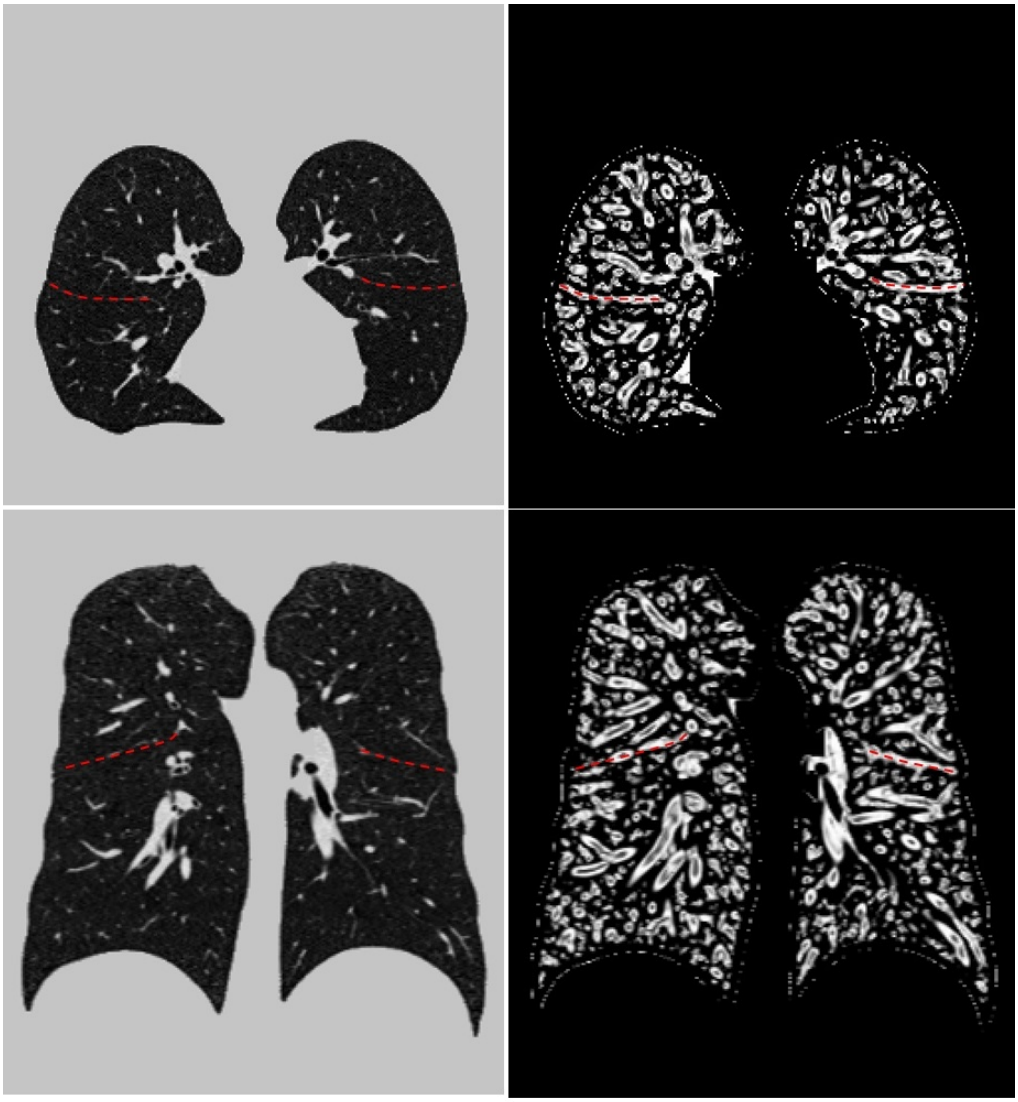

Figure 3.6: Extracted fissure-like structure in TLC. The upper row shows the transverse plane, and the lower row shows the coronal plane, (a) shows the corresponding CT image, and (b) shows the extracted fissure-like structure. The red dotted line represents the location of the fissure.

on the sheet-likeness shapes. However, Cao et al. suggest vesselness as an additional cost function, and they achieve enhanced registration accuracy [7, 8]. Therefore, we decided to keep the extracted vessel walls. The sheet-likeness measurement image is normalized to have a value from 0 to 1 because we can consider the sheet-likeness measurement as a probability function. In this sheet-likeness image, a higher value means that there is a high probability to be classified as a sheet-like structure, and a lower value means that there is a lower probability of this classification. The cost function for the sheet-likeness measurement can be defined as

$$Sheet = \int_{x \in \Omega} [S_T(x) - S_M(h(x))]^2 \tag{3.9}$$

where Ω denotes the overlaid region of the two images, S_T and S_M denote the sheet-likeness measurement of the target and moving image, respectively, and $h()$ denotes the transformation.

The final cost function of registration is

$$C = \alpha SSTVD + \beta Sheet + \gamma Reg \tag{3.10}$$

where α, β, and γ are user defined weight constants. In this thesis, we use $\alpha = 1$, $\beta = 1$, and $\gamma = 0.5$. Reg is a regularization term which is Laplacian. The regularization term is used to smooth the transformation, and helps reduce the unexpected changes in the displacement fields.

3.4 Optimization

To maximize the similarity function of the two images, it is necessary to find the optimal values and iteration numbers which maximize the correspondence of the two images. According to Hill et al. [20], these optimization problems are difficult to solve because calculating the optimal transformation can easily be converged to the local minima or maxima. Avoiding the local minima or maxima is a difficult issue in the registration. There are many algorithms to optimize the similarity measurement, such as the conjugate gradient based method (e.g. Fletcher-Reeves) and quasi-Newton based method (e.g. Limited-memory Broyden-Fletcher-Goldfarb-Shanno (L-BFGS)) [34]. We choose L-BFGS algorithm as an optimizer because L-BFGS is a good optimization algorithm for a high degree of freedom parameters.

3.5 Landmark error

Landmarks are feature points of the object. Landmarks are selected from the bifurcation points of the vascular tree. These points have good features to verify registration accuracy because the vessel bifurcation points keep the structural location during the respiratory cycle. The Euclidean distance between the landmark points is called landmark error. Landmark error (L) can be calculated as

$$L = \sum_{i}^{N} \sqrt{(A_i - B_i)^2} \tag{3.11}$$

where A_i denotes landmark points in the fixed image, and B_i denotes landmark points in the moving image. These landmark points are well distributed in the image pairs.

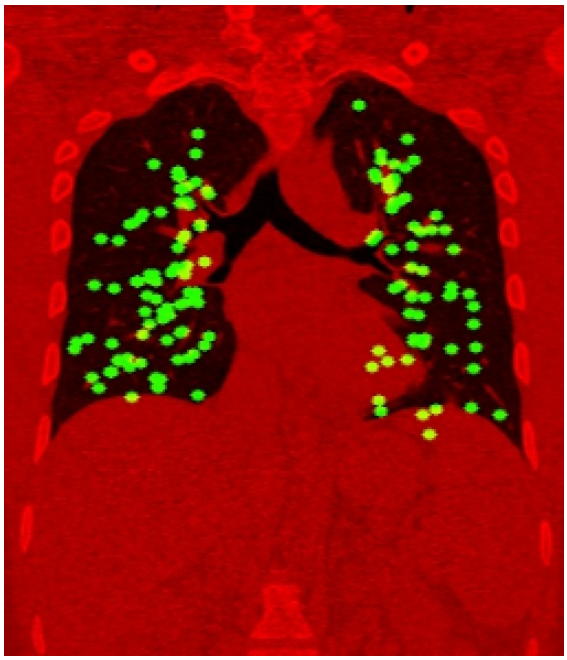

Figure 3.7: Distribution of the landmark points in the FRC image. Green dots represent each landmark point. Although green dots appear to the outside of the lung, they are located inside of the lung in 3D space. More than 100 well distributed points are used for each data pair.

Each i-th landmark point between the fixed and moving image corresponds with each other. Figure 3.7 shows the distribution of the landmark points.

Table 3.3 shows the initial landmark error (before registration) and lung volume ratio between FRC and TLC in every data set. Large mean landmark error represents that there are large displacements, and the larger volume ratio signifies an increased in volume change between FRC and TLC.

Table 3.3: The initial landmark error (before registration) and volume ratio between the FRC and TLC image

Subject	Mean landmark error (before)	Volume ration (TLC/FRC)
H-1	26.49 mm	1.96
H-2	25.54 mm	1.75
H-3	25.06 mm	1.79
H-4	25.54 mm	1.89
H-5	27.75 mm	1.91
H-6	31.53 mm	2.15

CHAPTER 4
EXPERIMENT RESULTS

The registration accuracy measurement is based on two different methods: a visual assessment and a landmark error measurement. We also compare the differences between the SSVMD and the sheet-likeness cost function.

4.1 Visual assessment

Registration accuracy can be assessed by the visual comparison of the fixed image and deformed moving image. Figure 4.1 shows the comparison between before and after the registration process. Figure 4.1 (d) shows initial volume differences before the registration is applied. Bright intensity regions represent large intensity differences, and dark intensity regions represent small or no intensity differences between the two images. Large bright regions are mainly observed at the bottom of the lung areas. However, figure 4.1 (e) shows small intensity differences. Theoretically, if the two images match completely, there are no intensity differences between the two images. Nevertheless, there are initial intensity differences between the FRC and TLC images due to the density differences at the different pressures of the lung. We can observe that the high contrast regions, such as vessels, are matched well.

4.2 Landmark error

Landmarks are useful to assess registration accuracy, as mentioned in Chapter 3. To verify registration accuracy, more than 100 landmark points are used for each

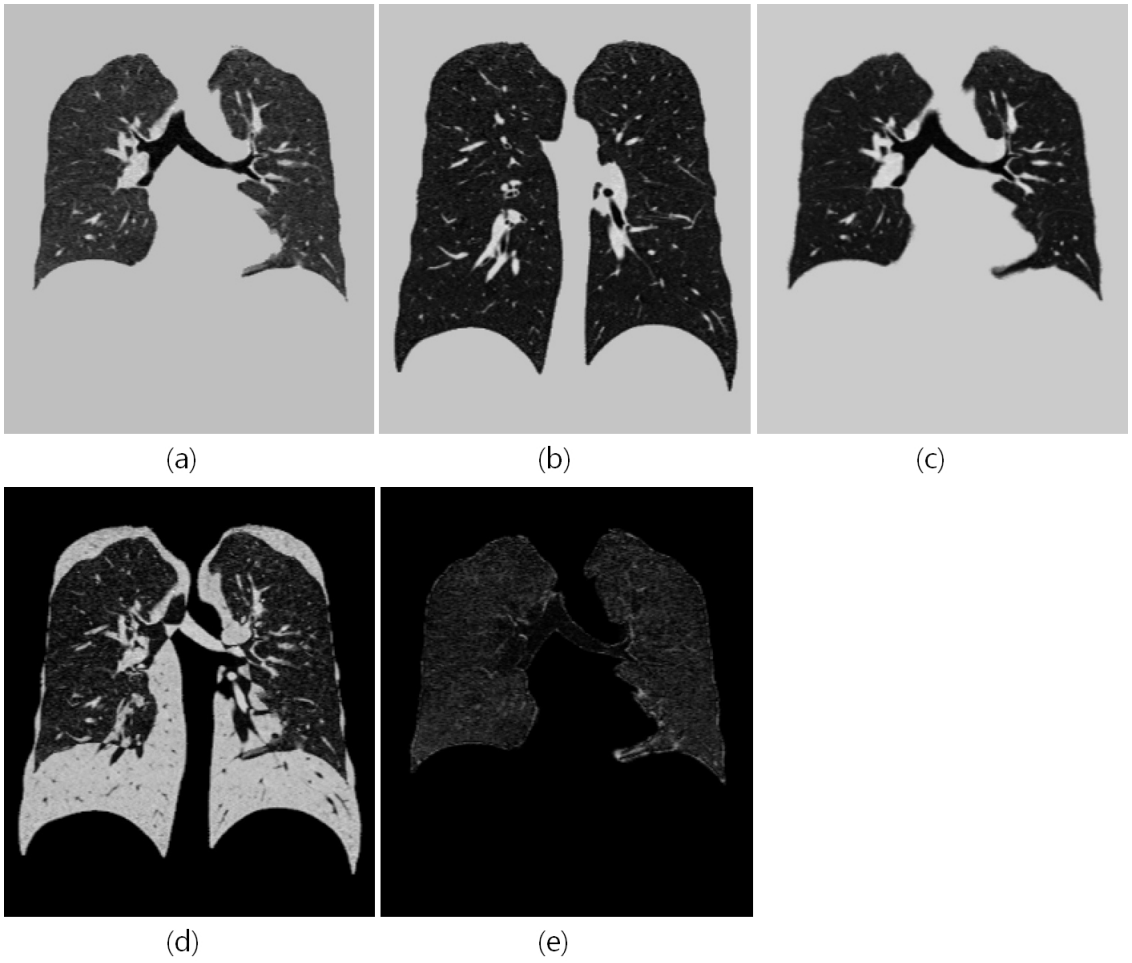

Figure 4.1: Comparison between before and after registration. (a) shows the fixed image (FRC) of subject H-1, (b) shows the moving image (TLC), (c) shows the deformed moving image (registration result), (d) shows the absolute difference image between the fixed and moving image, and (e) shows the absolute difference image between the fixed image and deformed moving image. All images are taken in the coronal plane.

pair. Mean, minimum, and maximum landmark error are calculated. In addition to these errors, the accumulated landmark error histogram is also used to see how many errors are located below a certain percentile. Table 4.1 shows the mean landmark error before and after registration with sheet-likeness.

In table 4.1, we can calculate that the average registration error is 1.42 mm. Since we use a half-size image to increase the registration speed, the input image voxel spacing is approximately 1.3 mm. Mean landmark error is approximately one voxel distance in average. The mean landmark errors after registration are close to 1 mm except the H-6 data pair. The H-6 data set has a large error than the other data pairs because the H-6 volume pair has the largest volume changes at the EE and EI.

Table 4.1: Mean landmark between before and after the registration with sheet-likeness

	Before registration	After registration
H-1	26.49 mm	1.16 mm
H-2	25.54 mm	1.17 mm
H-3	25.06 mm	0.87 mm
H-4	25.54 mm	0.95 mm
H-5	27.75 mm	1.04 mm
H-6	31.53 mm	3.33 mm

4.3 Comparison between cost functions

We propose the sheet-likeness measurement in terms of an additional cost function of the lung CT image registration. To prove the superiority of the proposed

algorithm, we compare our results with those of the previous study which uses the SSTVD and the SSVMD. Since the SSVMD uses vessel-like structure as an additional cost function, we prove the registration accuracy enhancement of our study by comparing landmark errors of our method, which is the combination of the SSTVD and the sheet-likeness, to the SSTVD only, the combination of the SSTVD and SSVMD. The experiment is performed in multiple times with the same subjects and the same registration parameters. The only difference is the cost function that is used. Table 4.2, 4.3, and 4.4 represent mean, minimum, and maximum landmark errors for each method.

Table 4.2: Mean landmark error comparison between before and after the registration with various methods (unit : mm)

	H-1	H-2	H-3	H-4	H-5	H-6
Before	26.49 (±12.35)	25.54 (±14.18)	25.06 (±13.18)	25.54 (±12.82)	27.75 (±13.45)	31.53 (±18.20)
only SSTVD	1.37 (±1.54)	1.44 (±1.25)	0.89 (±0.46)	1.26 (±1.43)	1.38 (±1.68)	3.84 (±4.26)
SSTVD+SSVMD	1.19 (±1.10)	1.16 (±0.49)	0.86 (±0.46)	0.91 (±0.50)	1.12 (±1.10)	3.89 (±4.66)
SSTVD+Sheet	1.16 (±0.98)	1.17 (±0.50)	0.87 (±0.46)	0.95 (±0.56)	1.04 (±0.53)	3.33 (±4.02)

Table 4.3: Minimum landmark error comparison between before and after the registration with various methods (unit : mm)

	H-1	H-2	H-3	H-4	H-5	H-6
Before	5.38	4.79	5.82	4.57	5.53	3.11
only SSTVD	0.16	0.24	0.03	0.14	0.13	0.36
SSTVD+SSVMD	0.15	0.15	0.12	0.12	0.09	0.35
SSTVD+Sheet	0.17	0.15	0.08	0.21	0.17	0.27

Table 4.4: Maximum landmark error comparison between before and after the registration with various methods (unit : mm)

	H-1	H-2	H-3	H-4	H-5	H-6
Before	59.44	62.43	62.29	52.45	55.48	72.91
only SSTVD	12.30	10.78	3.17	8.67	14.88	19.43
SSTVD+SSVMD	9.76	3.33	3.17	3.66	13.57	20.08
SSTVD+Sheet	8.40	3.13	3.04	3.94	3.48	18.48

Figure 4.2 shows the bar chart of the landmark error before registration and figure 4.3 shows the bar chart of the landmark error after registration.

According to table 4.2, there are large landmark error differences between the only SSTVD method and the combined methods. The average mean landmark error is 1.70mm for only the SSTVD, 1.52mm for the SSTVD and SSVMD, 1.42mm for the SSTVD and sheet-likeness. As you can see in this table, we can observe lager mean landmark errors in the SSTVD only method compared to the combination

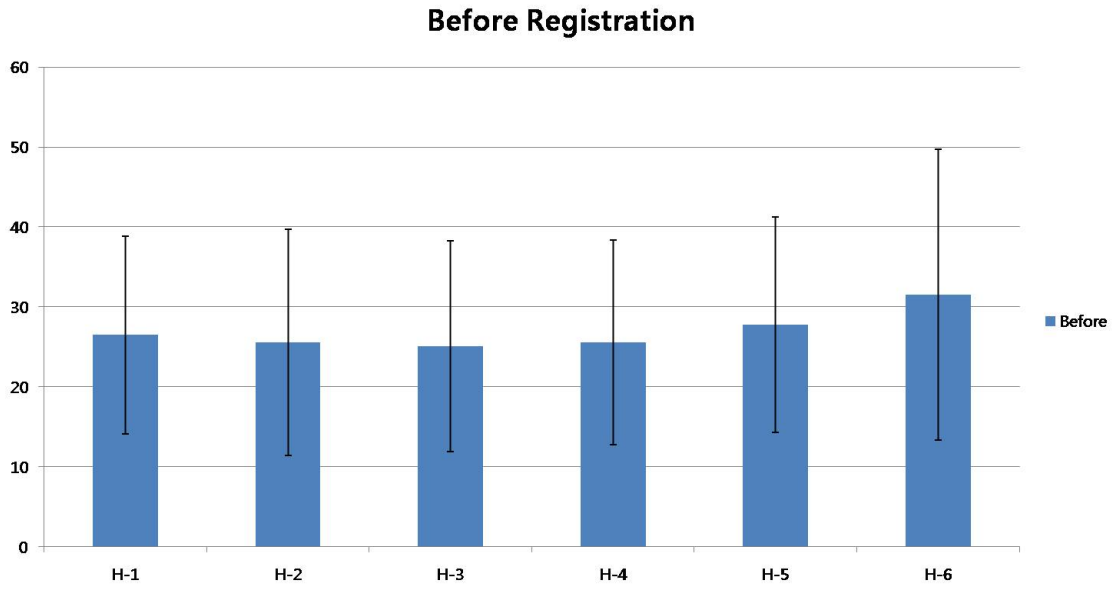

Figure 4.2: Landmark error before registration showing standard deviation (unit : mm).

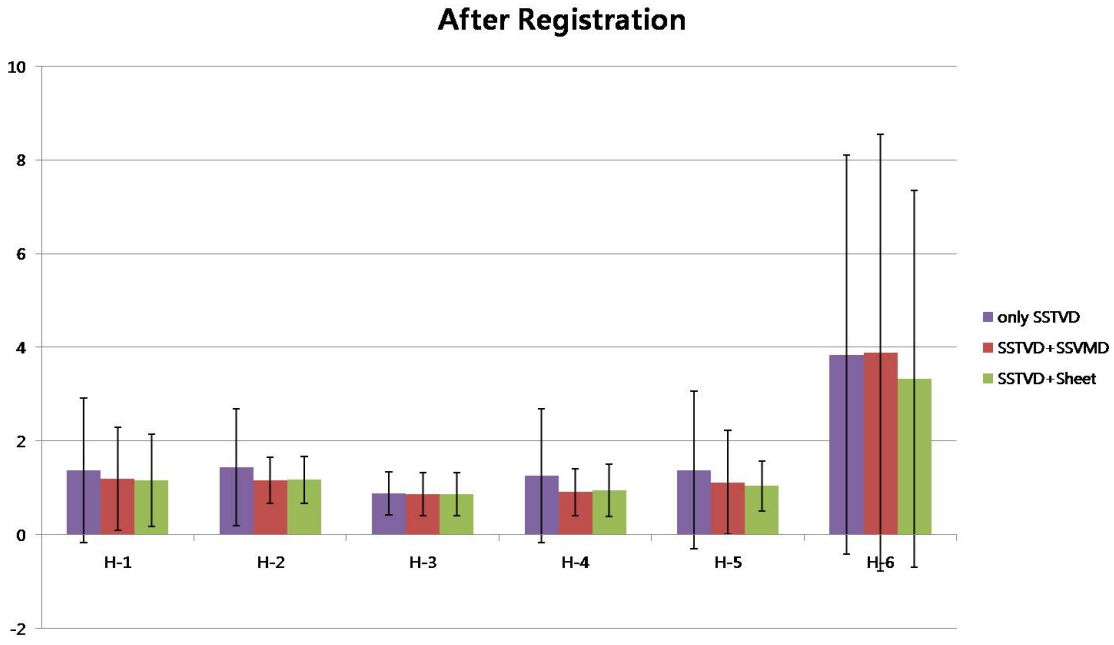

Figure 4.3: Landmark error after registration showing standard deviation for the three different cost functions (unit : mm).

of the SSTVD and SSVMD and the combination of the SSTVD and sheet-likeness. There is statistical significance between the SSTVD only and the combination of the SSTVD and SSVMD in the data pairs of H-2, H-4 and H-5 ($p < 0.05$). There is also statistical significance between the SSTVD only and the combination of the SSTVD and sheet-likeness in the data pairs of H-2, H-4 and H-5 ($p < 0.05$). There is no statistical significance in some data sets, and the reason is that the SSTVD only method can achieve small landmark errors as well as the combined methods (for H-1 and H-3) or every algorithm fails to reduce landmark errors which means the registration result has large landmark errors(for H-6). Table 4.3 shows the minimum landmark error for the three methods. The average minimum landmark error is 0.177mm for the only SSTVD, 0.163mm for the SSTVD and SSVMD, and 0.175mm for the SSTVD and sheet-likeness. The best result is observed from the combination of the SSTVD and SSVMD. 4.4 shows the maximum error for three methods. The average maximum landmark error is 11.538mm for the only SSTVD, 8.928mm for the SSTVD and SSVMD, and 6.745mm for the SSTVD and sheet-likeness. The best results of the landmark errors are observed from the combination of the SSTVD and sheet-likeness. For more detail results, in the appendix section, accumulated landmark error histograms and box plots are available to compare these three cost functions.

However, since the landmark points are located on vessel bifurcation points, the landmark errors may not be enough to represent the advantage of the sheet-likeness method. To further show the advantage of our method, we provide the

comparison between the combination of the SSTVD and SSVMD and the combination of the SSTVD and sheet-likeness. Figure 4.4 shows the differences between the two methods. We use the segmented lobe image to show the differences between the results. In figure 4.4 (a), a little more red and green colors are observed than in figure 4.4 (b). In addition, the only difference in figure 4.4 (c) is observed near the fissure areas. If two images match perfectly, the fused image can be shown in yellow. However, it is difficult to determine the better method because there are minor differences near fissure areas, and it is difficult to prove lung parenchyma matching.

Figure 4.4: Fissure alignment differences between the SSVMD and the sheet-likeness in H-1. (a) shows the fused image between the segmented FRC image (red color based) and the deformed segmented TLC image by using the combination of the SSTVD and SSVMD (green color based), (b) shows the fused image between the segmented FRC image (red color based) and the deformed segmented TLC image by using the combination of the SSTVD and sheet-likeness (green color based), and (c) shows the fused image between the deformed TLC (moving) image between the combination of the SSTVD and SSVMD (green color) and the combination of the SSTVD and sheet-likeness. All images are taken in the transverse plane.

CHAPTER 5
DISCUSSION AND CONCLUSION

In this thesis, we suggest an additional cost function to improve lung CT image registration accuracy by adding an additional anatomical cost function. Registration accuracy of the lung CT image registration is an important issue. As shown by a previous study [31], the additional cost function of vesselness, which is based on the anatomical structure similarity measurement of the lung, can achieve improved registration accuracy. Inspired by the previous work [31], we think that fissures can be useful features for lung CT image registration. Since the fissures have a sheet-like shape, an eigenvalue-based shape detection filter is used to extract the sheet-like structure. However, there are some difficulties in segmenting fissures with the shape detection filter due to the low contrast and incompleteness. The registration accuracy measurement method is based on the landmark error which is the Euclidean distance of the vessel bifurcation points. However, the landmark error may not be enough to verify the internal tissue matching. Although the vessels matched well, the lung parenchyma may not match. We compare the differences between three lung CT image registration techniques based on the landmark error. We can observe the differences between three metrics. The SSTVD cost gives the worst result in average mean landmark error. The combination of the SSTVD and the SSVMD costs, and the combination of the SSTVD and the sheet-likeness costs have small differences in the landmark error. The combination of the SSTVD and sheet-likeness shows slightly better average mean and maximum landmark errors. However, the

deformation patterns between SSVMD and sheet-likeness show some differences. The most differences are observed near fissure areas. The sheet-likeness can align the fissures more than the combination of the SSTVD and SSVMD metric when we can detect fissures on the image. However, some data sets have incomplete fissures which are not detected. There are some limitations in the incomplete fissures with the sheet-likeness filter. In this case, more misalignments are observed near the fissure areas. In addition to the misalignment, there are possibilities that mismatched correspondences can cause errors during the registration process. To minimize mismatching, we do the experiments with various parameters such as user-defined weight factors of the cost functions. This thesis work presents an additional cost function which combined with the intensity based registration cost function. The intensity only based registration metric is not enough to match the internal tissues. By combining the intensity-based cost function (SSTVD) and anatomical structure based cost function (sheet-likeness), we can achieve better accuracy than previous studies. Improved registration accuracy can result in enhanced measurement accuracy of the mechanical analysis of the lung. A more detailed analysis method, such as the fissure alignment comparison, can help to verify the strength of our method.

APPENDIX A
ACCUMULATED LANDMARK ERROR

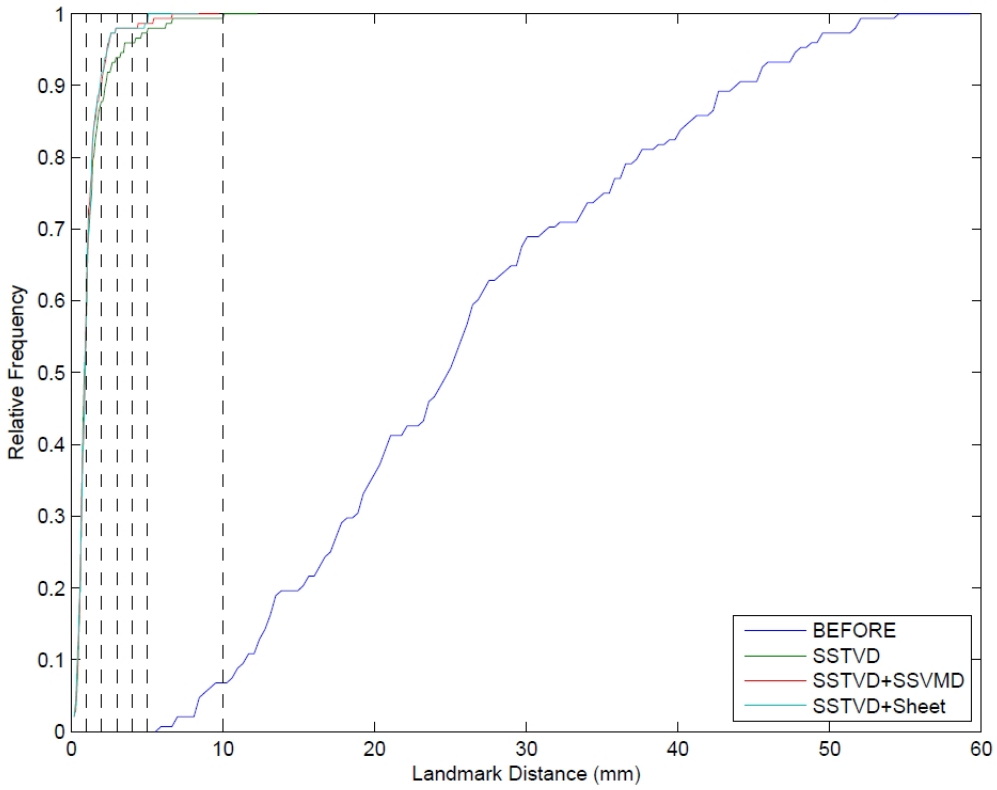

Figure A.1: Subject H-1. Comparison between before and after registration with three different cost functions.

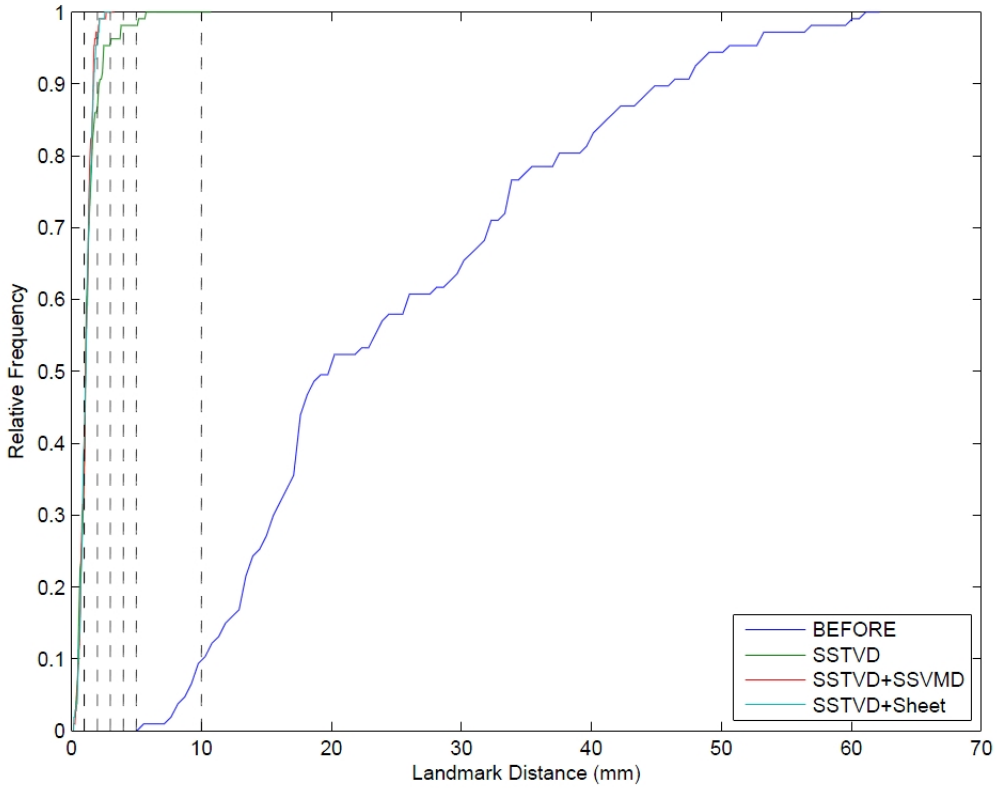

Figure A.2: Subject H-2. Comparison between before and after registration with three different cost functions.

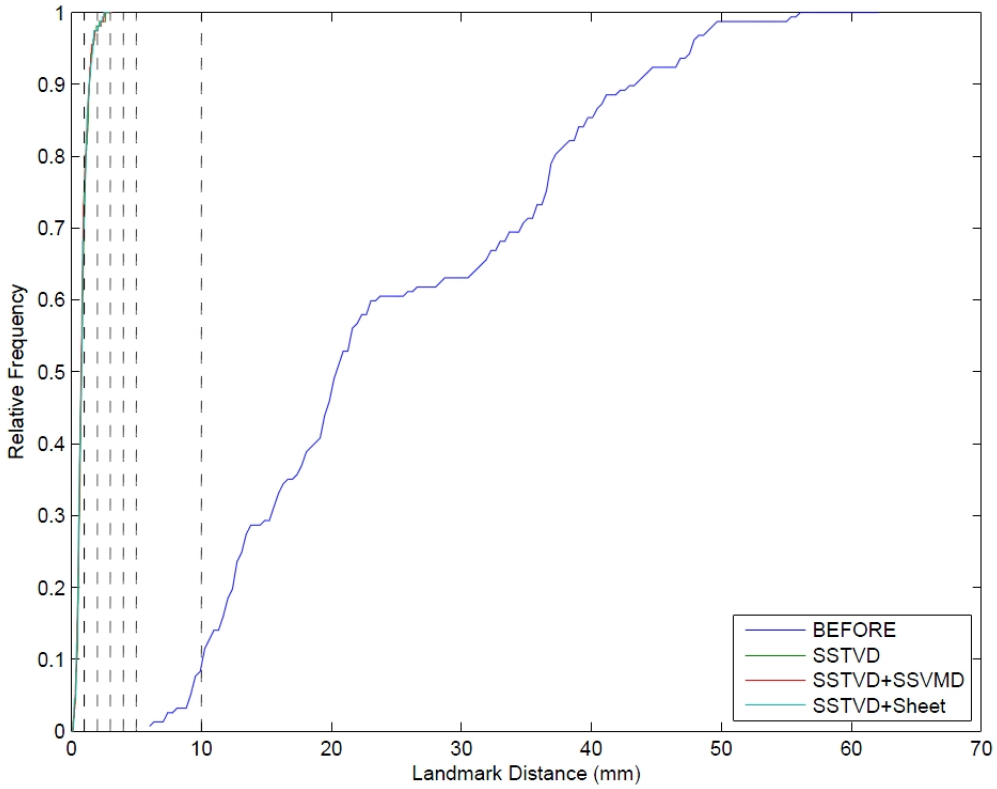

Figure A.3: Subject H-3. Comparison between before and after registration with three different cost functions.

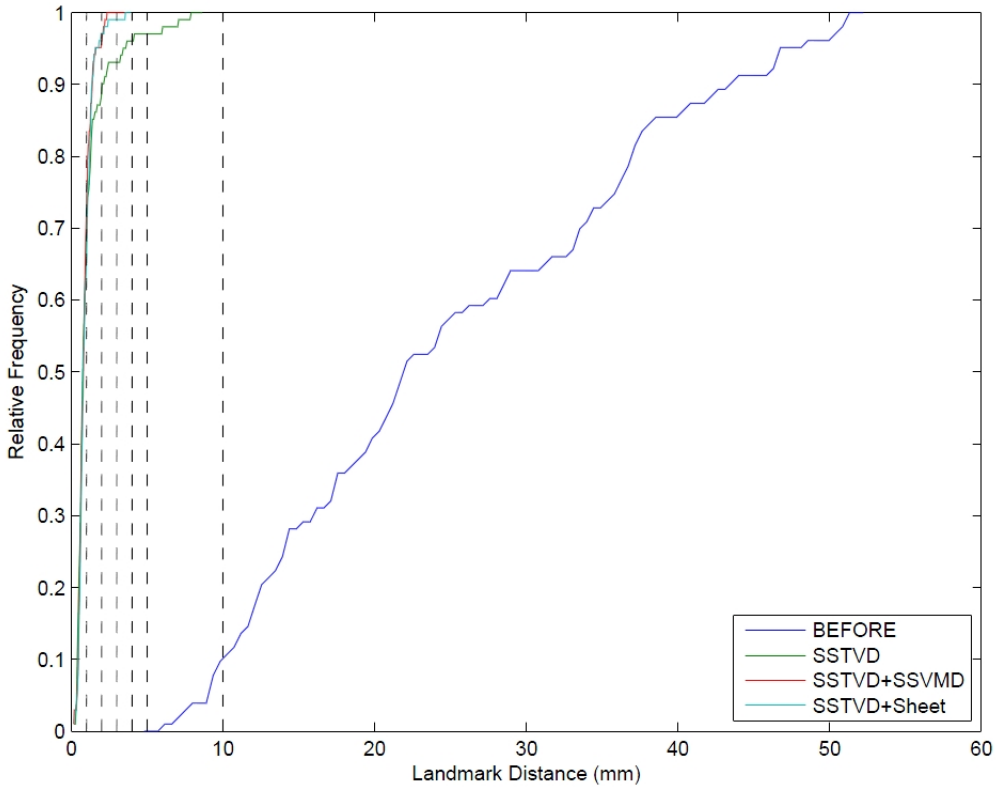

Figure A.4: Subject H-4. Comparison between before and after registration with three different cost functions.

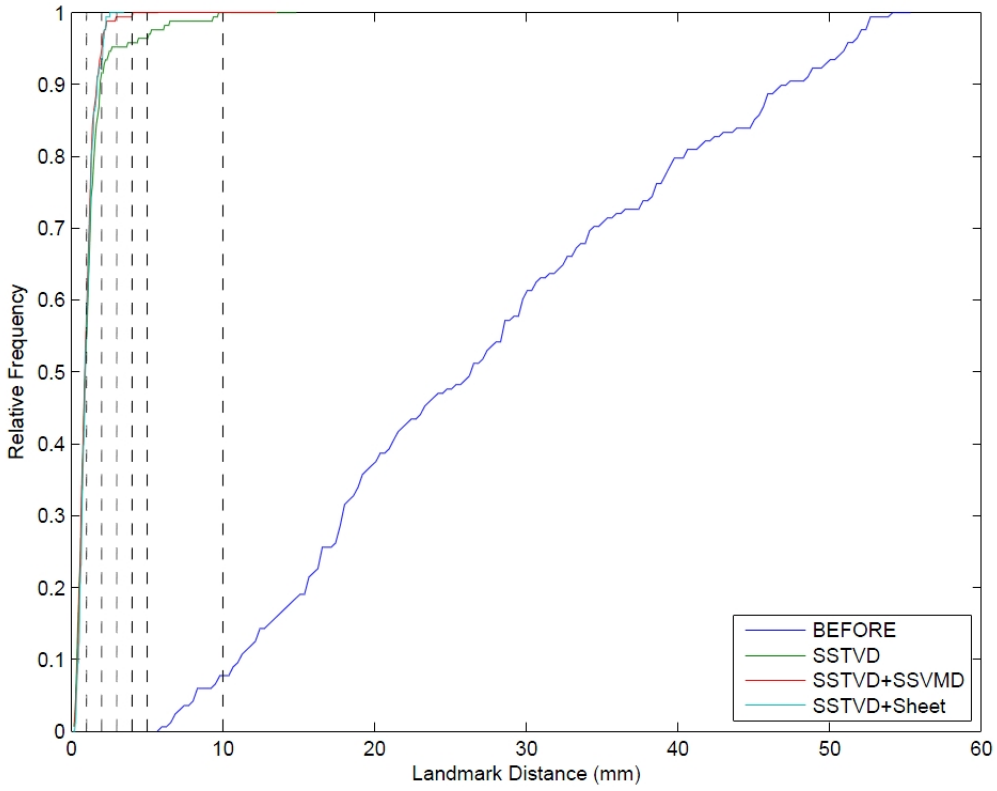

Figure A.5: Subject H-5. Comparison between before and after registration with three different cost functions.

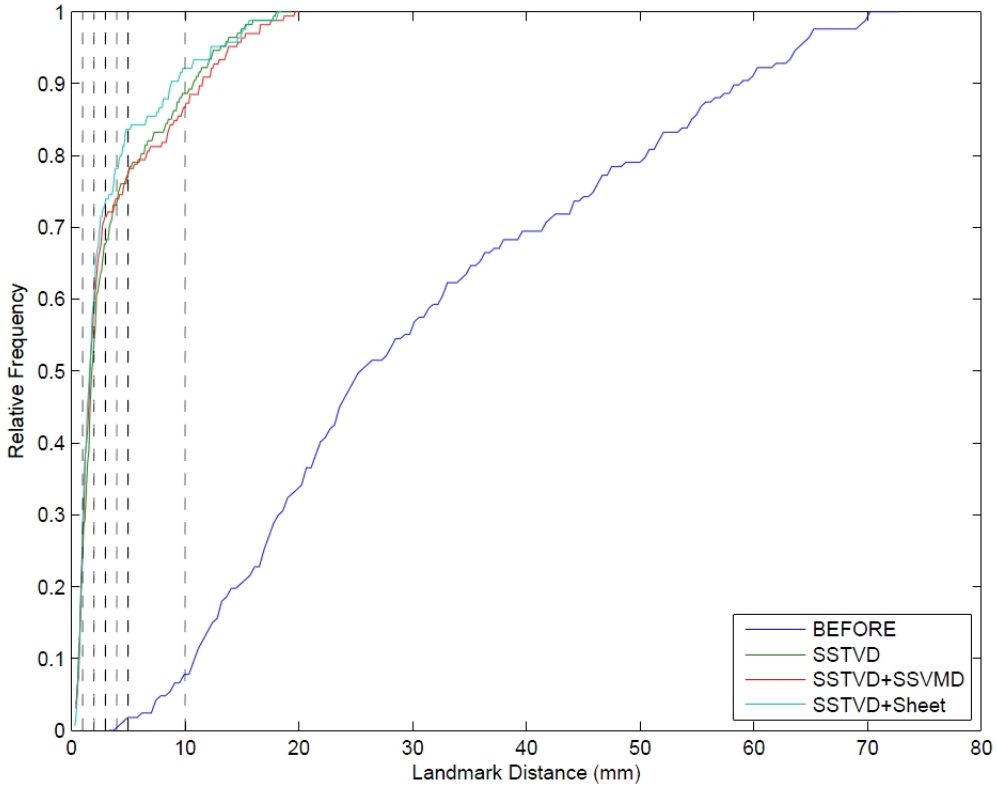

Figure A.6: Subject H-6. Comparison between before and after registration with three different cost functions.

APPENDIX B
BOX PLOT OF THE LANDMARK ERROR AFTER REGISTRATION

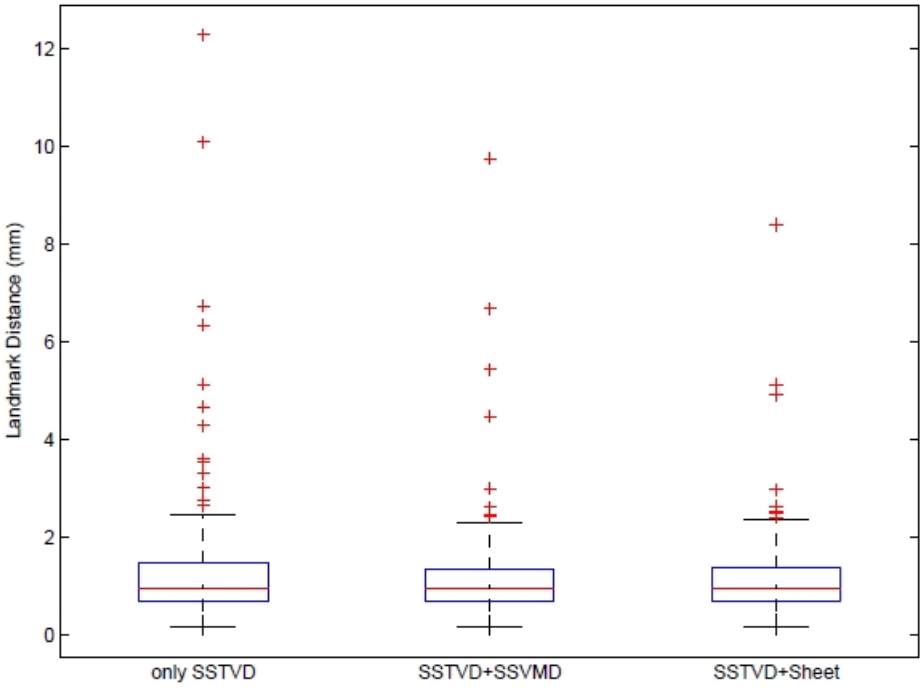

Figure B.1: Subject H-1. Box plot of the landmark error after registration with three different cost functions.

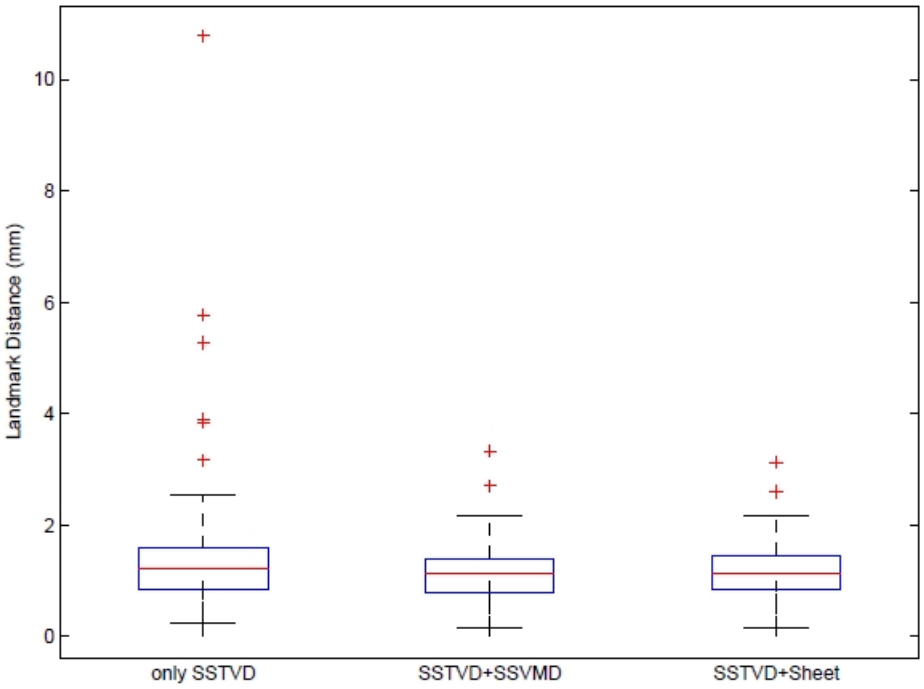

Figure B.2: Subject H-2. Box plot of the landmark error after registration with three different cost functions.

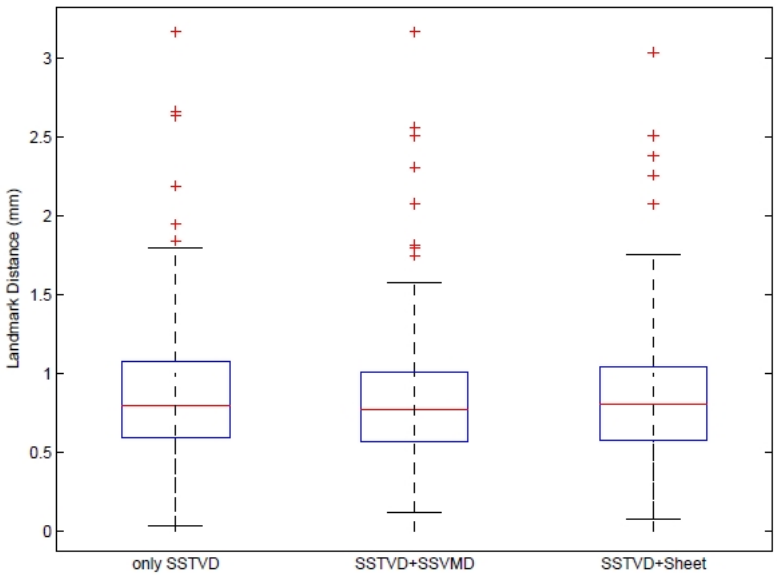

Figure B.3: Subject H-3. Box plot of the landmark error after registration with three different cost functions.

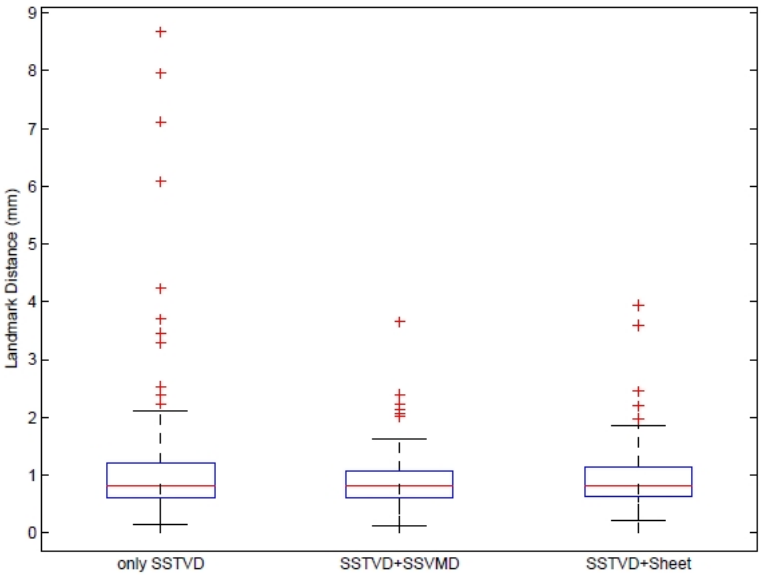

Figure B.4: Subject H-4. Box plot of the landmark error after registration with three different cost functions.

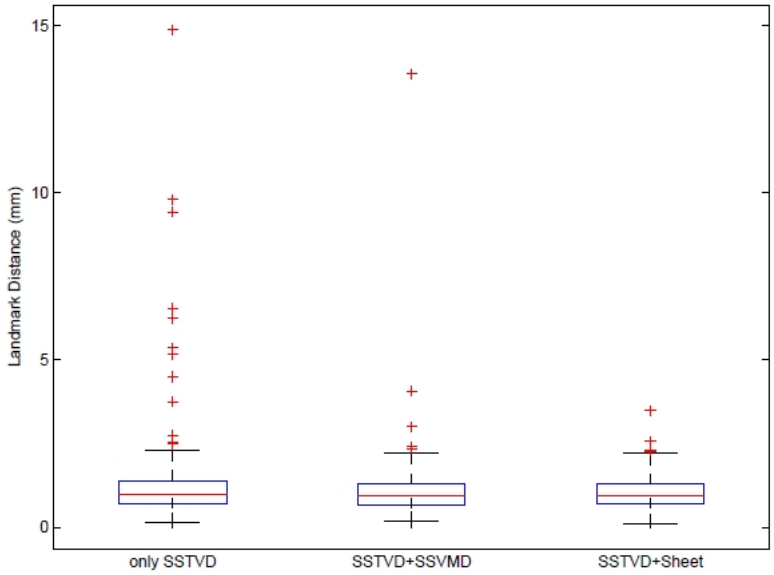

Figure B.5: Subject H-5. Box plot of the landmark error after registration with three different cost functions.

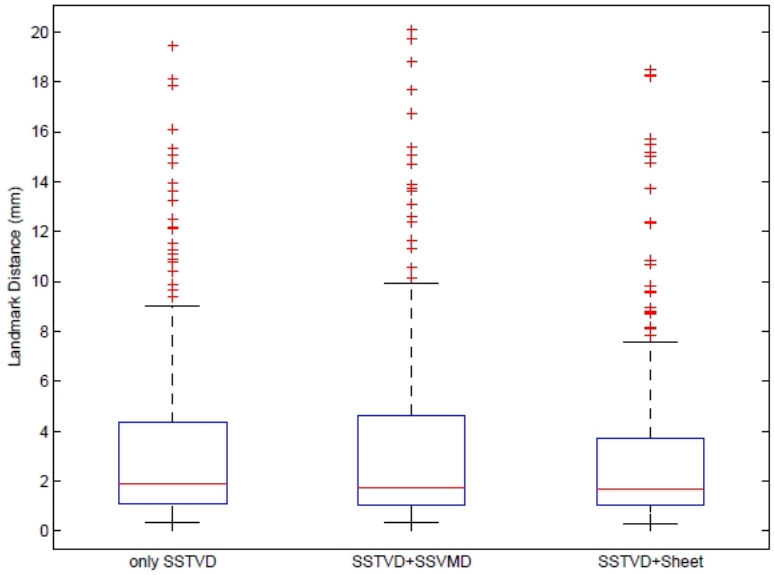

Figure B.6: Subject H-6. Box plot of the landmark error after registration with three different cost functions.

REFERENCES

[1] John B. West. Respiratory physiology : the essentials. *Lippincott Williams and Wilkins*, 9th edition, September 2011.

[2] Nicholas J. Tustison, Tessa S. Cook, Gang Song, and James C. Gee. Pulmonary kinematics from image data: A review. *Academic Radiology*, 18(4):402–417, 2011.

[3] Marius Staring, Stefan Klein, Johan H. C. Reibe, Wiro J. Niessen, and Berend C. Stoel. Pulmonary image registration with elastix using a standard intensity-based algorithm. *In EMPIRE10: MICCAI 2010 Workshop on Evaluation of Methods for Pulmonary Image Registration*, 2010.

[4] Lawrence Dougherty, Jane C. Asmuth, and Warren B. Gefter. Alignment of ct lung volumes with an optical flow method. *Academic Radiology*, 10(3):249–254, 2003.

[5] Xiao Han. Feature-constrained nonlinear registration of lung ct images. *In EMPIRE10: MICCAI 2010 Workshop on Evaluation of Methods for Pulmonary Image Registration*, 2010.

[6] Sven Kabus and Cristian Lorenz. Fast elastic image registration. *In EMPIRE10: MICCAI 2010 Workshop on Evaluation of Methods for Pulmonary Image Registration.*

[7] Kunlin Cao, Kai Ding, Gary E. Christensen, Madhavan L. Raghavan, Ryan E. Amelon, and Joseph M. Reinhardt. Unifying vascular information in intensity-based nonrigid lung ct registration. *In Proceedings of the 4th international conference on Biomedical image registration*, 2010.

[8] Kunlin Cao, Kaifang Du, Kai Ding, Joseph M. Reinhardt, and Gary E. Christensen. Regularized nonrigid registration of lung ct images by preserving tissue volume and vesselness measure. *In EMPIRE10: MICCAI 2010 Workshop on Evaluation of Methods for Pulmonary Image Registration*, 2010.

[9] Youbing Yin, Eric A. Hoffman, and Ching-Long Lin. Local tissue-weight-based nonrigid registration of lung images with application to regional ventilation. *Proceedings of SPIE*, 2009.

[10] Margrit Betke, Harrison Hong, and Jane P. Ko. Automatic 3d registration of

lung surfaces in computed tomography scans. *Medical Image Computing and Computer-Assisted Intervention*, pages 725–733, 2001.

[11] Sata Busayarat and Tatjana Zrimec. Ray-tracing based registration for hrct images of the lungs. *Medical Image Computing and Computer-Assisted Intervention*, pages 670–677, 2006.

[12] Alexander Schmidt-Richberg, Jan Ehrhardt, Rene Werner, and Heinz Handels. Diffeomorphic diffusion registration of lung ct images. *In EMPIRE10: MICCAI 2010 Workshop on Evaluation of Methods for Pulmonary Image Registration*, 2010.

[13] Sascha E.A. Muenzing, Bram van Ginneken, and Josien P.W. Pluim. Knowledge driven regularization of the deformation field for pde based non-rigid registration algorithm. *In EMPIRE10: MICCAI 2010 Workshop on Evaluation of Methods for Pulmonary Image Registration*, 2010.

[14] Marc Modat, Jamie McClelland, and Sebastien Ourseli. Lung registration using the niftyreg package. *In EMPIRE10: MICCAI 2010 Workshop on Evaluation of Methods for Pulmonary Image Registration*, 2010.

[15] K. Keelin et al. Evaluation of registration methods on thoracic ct : The empire10 challenge. *In EMPIRE10: MICCAI 2010 Workshop on Evaluation of Methods for Pulmonary Image Registration*, 2010.

[16] J. Michael Fitzpatrickr, Derek L. G. Hill, and Jr. Calvin R. Maurer. Handbook of medical imaging. medical image processing and analysis. *SPIE*, 2(Chapter 8):447–513, 2000.

[17] J. B. Antoine Maintz and Max A. Viergever. A survey of medical image registration. *Medical Image Analysis*, 2(1):1–36, 1998.

[18] D. Chetverikov, D. Svirko, D. Stepanov, and P. Krsek. The trimmed iterative closest point algorithm. *Object recognition supported by user interaction for service robots. IEEE Comput. Soc.*, 2002.

[19] Kunlin Cao, Kai Ding, Joseph M. Reinhardt, and Gary E. Christensen. Improving intensity-based lung ct registration accuracy utilizing vascular information. *International Journal of Biomedical Imaging*, 2012, 2012.

[20] Derek L G Hill, Philipp G Batchelor, Mark Holden, and David J Hawkes. Medical image registration. *Physics in medicine and biology*, 46(3), 2001.

[21] Jeongtae Kim and Jeffrey A. Fessler. Image registration using robust correlation. *Proceedings IEEE International Symposium on Biomedical Imaging*, 2002.

[22] C. Studholme, D. Hill, and D. Hawkes. An overlap invariant entropy measure of 3d medical image alignment. *Pattern Recognition*, 32(1):71–86, 2002.

[23] Josien P. W. Pluim, J. B. Antoine Maintz, and Max A. Viergever. Mutual-information-based registration of medical images: a survey. *Pattern Recognition*, 22(8):986–1004, aug 2003.

[24] elastix. http://elastix.isi.uu.nl/.

[25] Xiao Han, Lyndon S. Hibbard, and Virgil Willcut. Gpu-accelerated, gradient-free mi deformable registration for atlas-based mr brain image segmentatio. *IEEE Computer Society Conference on Computer Vision and Pattern Recognition Workshops*, 2012.

[26] Alejandro F. Frangi, Wiro J. Niessen, Koen L. Vincken, and Max A. Viergever. Multiscale vessel enhancement filtering. *Medical Image Computing and Computer-Assisted Intervention*, 1496(3):130–137, 1998.

[27] Michael Kass, Andrew Witkin, and Demetri Terzopoulos. Snakes : Active contour models. *International Journal of Computer Vision*, 1(4):321–331, 1988.

[28] Jan Ehrhardt, Rene Werner, Alexander Schmidt-Richberg, and Heinz Handels. Automatic landmark detection and non-linear landmark- and surface-based registration of lung ct images. *Medical Image Computing and Computer-Assisted Intervention*, 2010.

[29] Tom Vercauteren, Xavier Pennec, Aymeric Perchant, and Nicholas Ayache. Non-parametric diffeomorphic image registration with the demons algorithm. *Medical Image Computing and Computer-Assisted Intervention*, 10(Pt 2):319–326, 2007.

[30] S. Ourselin, A. Roche, G. Subsol, and X. Pennec N. Ayache. Reconstructing a 3d structure from serial histological sections. 19:25–31, 2001.

[31] Kunlin Cao. Mechanical analysis of lung ct images using nonrigid registration. *Theses and Dissertations, University of Iowa*, 2012.

[32] Yoshinobu Sato, Carl-Fredrik Westin, Abhir Bhalerao, Shin Nakajima, Nobuyuki Shiraga, Shinichi Tamura, and Ron Kikinis. Tissue classification based on 3d local intensity structures for volume rendering. 6(2):160–180, 2000.

[33] Luca Antiga. Generalizing vesselness with respect to dimensionality and shape. *The Insight Journal*, 2007.

[34] William H. Press, Saul A. Teukolsky, William T. Vetterling, and Brian P. Flannery. Numerical recipes in c (2nd ed.): the art of scientific computing. *Cambridge University Press New York*, 1992.